Decoupling the electronic gap from the spin Chern number in spin-resolved topological insulators

Alexander C. Tyner,[1,2] Cormac Grindall,[3] and J. H. Pixley[3,4]

[1]*Nordita, KTH Royal Institute of Technology and Stockholm University, 106 91 Stockholm, Sweden*

[2]*Department of Physics, University of Connecticut, Storrs, Connecticut 06269, USA*

[3]*Department of Physics and Astronomy, Center for Materials Theory, Rutgers University, Piscataway, New Jersey 08854, USA*

[4]*Center for Computational Quantum Physics, Flatiron Institute, 162 5th Avenue, New York, New York 10010, USA*

(Received 29 March 2024; revised 20 August 2024; accepted 26 November 2024; published 27 December 2024)

In two-dimensional topological insulators, a disorder-induced topological phase transition is typically identified with an Anderson localization transition at the Fermi energy. However, in $\mathbb{Z}_2$ trivial, spin-resolved topological insulators it is the spectral gap of the spin spectrum, in addition to the bulk mobility gap, which protects the nontrivial topology of the ground state. In this work, we show that these two gaps, the bulk electronic and spin gap, can evolve distinctly on the introduction of quenched short-ranged disorder and that an odd-quantized spin Chern number topologically protects states below the Fermi energy from localization. This decoupling leads to a unique situation in which an Anderson localization transition occurs below the Fermi energy at the topological transition. Furthermore, the presence of topologically protected extended bulk states nontrivial bulk topology typically implies the existence of protected boundary modes. We demonstrate the absence of protected boundary modes in the Hamiltonian and yet the edge modes in the eigenstates of the projected spin operator survive. Our work thus provides evidence that a nonzero spin-Chern number, in the absence of a nontrivial $\mathbb{Z}_2$ index, does not demand the existence of protected boundary modes at finite or zero energy.

DOI: 10.1103/PhysRevB.110.214211

I. INTRODUCTION

Understanding the robustness of topological properties to weak perturbations in electronically gapped systems has remained a central question at the forefront of research in condensed-matter physics [1–6]. The destruction of topological properties on closing the electronic gap is a fundamental concept underlying this phenomena in a wide range of physical systems such as a two-dimensional electron gas in a magnetic field (e.g., the integer [1] and fractional [7,8] quantum Hall effects) and topological band structures such as Chern [9] and topological insulators [3]. On the introduction of weak disorder (that does not break any protecting symmetry such as time reversal in the case of $\mathbb{Z}_2$ topological insulators), this electronic gap closes (being filled in by Anderson localized Lifshitz states [10,11]) but so long as the mobility gap remains open, the topological properties can be rigorously proven to remain intact [3–5,12–24]. As a consequence, the bulk mobility gap is always used as a metric of how "protected" the ground-state topology is to external perturbations [5,6,14].

In quantum spin Hall insulators this same paradigm has been widely adopted. However, the presence of nontrivial spin-resolved topology requires the preservation of a gap in both the electronic and spin spectrum [25]. A gapped spin spectrum is essential as the spin-Chern number (C_s) is a relative invariant. between the up and down spin sectors [4,12,25]; if the spin spectrum is gapless, then the up and down sectors can hybridize and trivialize the invariant. In the presence of disorder, these gaps are converted into mobility gaps, i.e., their spectrum is soft but their eigenstates are localized such that they remain insulators with regards to transport.

In many prominent cases the bulk spin mobility gap mirrors that of the bulk electronic mobility gap in the presence of disorder. This is true of $\mathbb{Z}_2$ nontrivial spin-Hall insulators [4,15,25]. It is also true in higher-order or crystalline topological insulators, provided the disorder does not violate the crystalline symmetries protecting the bulk topology [26–44]. It has therefore been common practice to ignore the spin gap altogether and only study the electronic spectrum.

Here we show that in spin-resolved topological insulators that lack a nontrivial $\mathbb{Z}_2$ index but support a quantized C_s it is essential to study both the electronic and spin spectrum concomitantly. By generalizing the typical density of states to the spin spectrum we show that it is possible to decouple the fate of the electronic and spin mobility gaps as a function of disorder. While the disorder driven topological spin Hall-to-trivial insulator phase transitions can be identified by the spin gap closing at the Fermi energy, in direct contrast with all of the other paradigmatic examples we have previously discussed, the electronic mobility gap does not close at the Fermi energy. Instead, we provide strong numerical evidence through simulations on large system sizes that an Anderson

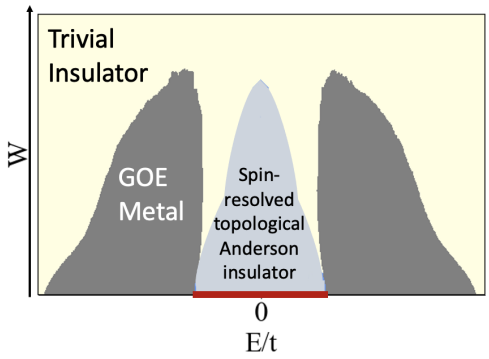

FIG. 1. Schematic bulk phase diagram of the disordered Hamiltonian in Eq. (1) as a function of energy E and strength of the random on-site disorder W. The higher-order topological phase, which is only stable in the clean limit ($W = 0$) is marked by a bold red line. The metallic bands at finite energy (shown in dark gray) are described by the Gaussian orthogonal ensemble (GOE) of random matrix theory [45], which localizes at sufficiently large disorder without closing the mobility gap between the two bands. When the Fermi energy is placed within the light blue region such that the spin gap is intact, the spin Chern number is quantized and the system exhibits a spin-resolved Anderson topological insulator. The line separating the light yellow and light blue regions is the spin mobility edge that is decoupled from the electronic mobility edge that separates the gray and yellow regions. When all of the bulk states localize, the spin mobility gap closes and the spin-Chern number is no longer quantized.

localization transition takes place below the Fermi energy, leading to the phase diagram seen in Fig. 1, which is fundamentally distinct from known topological counterparts.

A major consequence of decoupling the electronic and spin mobility gaps must appear in the nature of edge modes as a result of the bulk-boundary correspondence.

In this work we utilize a two-dimensional band structure that hosts two distinct, spin-resolved topological insulating phases admitting $C_s = 1$ as well as a trivial insulating phase, $C_s = 0$. The two spin-resolved topological insulating phases are distinguished by the simultaneous presence of higher-order topology in one. We utilize these two topological band structures to show that higher-order topology is not necessary to realize the phenomena we study in this work. Nonetheless, as spin-resolved topology has been shown to commonly coexist with higher-order topology [46–51], higher-order insulators constitute ideal experimental candidates to realize disordered spin-resolved topological insulators.

As the higher-order topology of the model we study is symmetry protected, the introduction of disorder removes these symmetries but does not remove the quantized spin Chern number and it is therefore far from obvious what topological properties remain robust, answering this question is one major goal of the current work. We demonstrate that extended boundary modes protected by the bulk topology are absent. Nonetheless, the projected spin-operator does yield well-defined one-dimensional dispersing edge modes localized to their boundary provided the spin Chern number remains quantized. In addition, the electronic spectrum is shown to support topological surface modes only on an inserted zero dimensional defect [52,53].

Importantly, in the landmark work on the spin Chern number [25], Prodan noted "the existence of Chern numbers for different [spin] sectors does not automatically imply the existence of chiral edge modes." While it has been established that helical edge states need not be present when $\mathbb{Z}_2 = 0$ and $C_s \neq 0$, our result serves as a direct demonstration that the existence of a spin-Chern number, in the absence of a nontrivial $\mathbb{Z}_2$ index, does *not* dictate the existence of any protected boundary modes, whether at finite or zero energy.

The remainder of the paper is organized as follows. In Sec. II the tight-binding model that we study is introduced as well as details of how disorder will be modeled. In Sec. II A the electronic structure and topological properties of the tight-binding model in the clean limit are given. In Sec. II B the computational tools utilized to examine the electronic and and topological properties of the tight-binding model in the presence of disorder are defined. In Sec. III the effects of disorder are investigated, first with respect to the bulk and surface electronic spectrum in Sec. III A. Subsequently in Sec. III B, the effects of disorder on the bulk and surface spin spectrum as well as topology of the spin spectrum are explored. Finally, before concluding in Sec. IV, we examine the use of magnetic flux tubes to probe the bulk topology of the spin spectrum via the electronic spectrum in Sec. III C. In the Appendix we provide further details investigating (a) the prevalence of finite-size effects in our determination of the phase boundaries, (b) the fate or corner-modes for systems admitting higher-order topology in the clean limit, and (c) the effects of disorder in an additional spin-resolved topological insulator lacking higher-order topology in the clean limit.

II. MODEL, SYMMETRIES, AND APPROACH

We consider a quintessential tight-binding model which, for a set of parameters, is a spinful generalization of the famous Benalcazar-Bernevig-Hughes model [54,55] admitting two distinct spin-resolved topological insulating phases and a trivial insulating phase as seen in Fig. 2.

We introduce a random onsite potential $V(\mathbf{r})$ to model quenched, short-range disorder realizing the Hamiltonian,

$$H = \sum_{\mathbf{k}} \psi^{\dagger}_{\mathbf{k}} H_0(\mathbf{k}) \psi_{\mathbf{k}} + \sum_{\mathbf{r}} \psi^{\dagger}_{\mathbf{r}} V(\mathbf{r}) \psi_{\mathbf{r}}, \tag{1}$$

where $\psi_{\mathbf{r}}$ is a four component spinor at site $\mathbf{r}$ (or Bloch momentum $\mathbf{k}$). The Hamiltonian belongs to class BDI [16,18,24] in the clean limit and class AI on introduction of finite disorder and is therefore expected to demonstrate localization of the electronic states on introduction of disorder.

The Bloch Hamiltonian $H_0(\mathbf{k})$ takes the form:

$$\begin{aligned} H_0(\mathbf{k})/t = &\sin k_x \sigma_1 \otimes \tau_1 + \sin k_y \sigma_1 \otimes \tau_2 \\ &+ M(\mathbf{k}) \sigma_3 \otimes \tau_0 + \Delta(\mathbf{k}) \sigma_2 \otimes \tau_0, \end{aligned} \tag{2}$$

where t has units of energy, $\sigma_{0,1,2,3}(\tau_{0,1,2,3})$ are the 2×2 identity matrix and three Pauli matrices respectively, operating on the spin (orbital) indices. We further define $M(\mathbf{k}) = \alpha(\cos k_x + \cos k_y) + \gamma$ and $\Delta(\mathbf{k}) = \Delta_0 + t_1(\cos k_x - \cos k_y)$, fixing $\gamma = 0.9$ throughout. Time-reversal symmetry $\mathcal{T}$, is

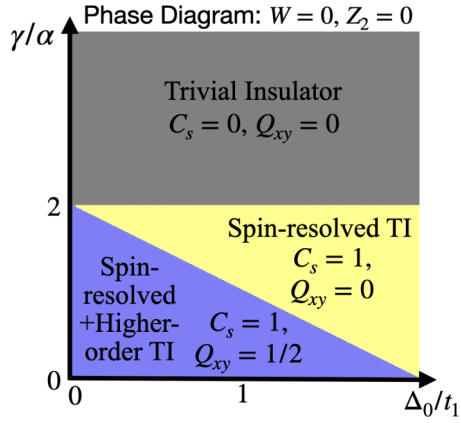

FIG. 2. Clean phase diagram: Topological phase diagram for the Hamiltonian in Eq. (2) in the clean limit ($W = 0$). A nontrivial Z_2 index cannot be defined for any phase. Two topologically nontrivial phases can be identified as a function of Δ_0/t_1 for $\gamma/\alpha < 2$. Both support spin-resolved topology, but a quantized quadrupole moment, $Q_{xy} = 1/2$, and zero-energy corner modes protected by chiral symmetry exist for $|\Delta_0/t_1| < |\gamma - 2\alpha|/|\alpha|$ as detailed in Ref. [56].

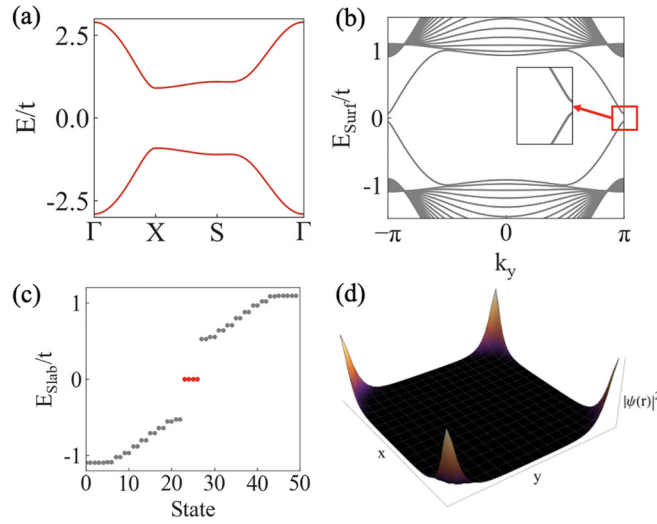

FIG. 3. Properties of the clean band structure: (a) Band structure along high-symmetry path for tight-binding model given by Eq. (2) for the parametr choice $\Delta_0 = 0$, $t_1 = 0.05$, and $\gamma/\alpha = 0.9$. (b) Spectra for a slab of 40 unit cells along the $\hat{x}$ direction and periodic boundary conditions along $\hat{y}$. Inset shows enlarged view of spectral gap at $k_y \pm \pi$. (c) Spectra of 50 lowest-lying states when applying open-boundary conditions along both principal axes in a systems of 50×50 unit cells. Localization of degenerate midgap states shown in red is detailed in (d), demonstrating that they are corner localized.

generated by $\mathcal{T}^\dagger H_0(-\mathbf{k})\mathcal{T} = H_0(\mathbf{k})$, where $\mathcal{T} = \sigma_3 \otimes \tau_1 \mathcal{K}$, where $\mathcal{K}$ represents complex conjugation. Additionally, a chiral symmetry, $S^\dagger H_0(\mathbf{k})S = -H_0(\mathbf{k})$ exists generated by $S = \sigma_1 \otimes \tau_3$ and particle-hole symmetry, generated by $\Sigma^\dagger H_0(\mathbf{k})\Sigma = -H_0(-\mathbf{k})$, where $\Sigma = \sigma_2 \otimes \tau_2 \mathcal{K}$.

At each site, we model the quenched disorder as a random onsite potential $V(\mathbf{r})$. We sample the potential $V(\mathbf{r})$ from a Gaussian distribution with zero mean and variance W^2, and hence W characterizes the strength of disorder. Throughout this work, W will be expressed in units of t.

In the following we present a detailed numerical study of the model defined in Eq. (1) through a combination of exact diagonalization that reaches up to linear system sizes $L = 60$ and the kernel polynomial method (KPM) [57] to study the average and typical density of states up to linear system sizes of $L = 1000$. Before describing the quantities and metrics we use to determine each phase of the system we begin with a review of the model in the clean limit [i.e., $V(\mathbf{r}) = 0$].

A. Clean limit

In the clean-limit Eq. (2) admits both spin-resolved and higher-order topological phases as a function of the model parameters, as seen in Fig. 2. More specifically, the higher-order topology observed in this model falls under the category of a boundary obstructed phase supporting bulk-corner correspondence when $\Delta_0 = 0$ and edge-corner correspondence for $\Delta_0 \neq 0$ [56,58]. While higher-order topology can be identified concomitantly with spin-resolved topology for a range of parameters, they are independent. Higher-order topology is not necessary to realize the physics investigated in this work. Nevertheless, HOTIs have been shown to be a natural place to identify two-dimensional, $Z_2 = 0$, spin-resolved topological insulators allowing for immediate connection to experimentally realized systems. We utilize, as starting points to study the effects of disorder, each phase shown in Fig. 2. In the main body we focus on the phase admitting higher-order and spin-resolved topology simultaneously as well as a topologically trivial phase. We further consider the spin-resolved topological phase in which higher-order topology is absent in Appendix C.

By fixing $\Delta_0 = 0, t_1 = 0.05$ and $\gamma/\alpha = 0.9$ the system at hand supports fourfold rotational symmetry generated by $C_4^\dagger H_0(k_x, k_y)C_4 = H_0(k_y, -k_x)$, where $C_4 = e^{-i\frac{\pi}{4}\tau_0\otimes\sigma_3} e^{-i\frac{\pi}{2}\tau_3\otimes\sigma_3}$, falling under the category of HOTIs with "bulk-corner" correspondence [56,58]. The bulk band structure along the high-symmetry path is shown in Fig. 3(a) detailing that the model is an insulator for our choice of parameters. Considering a cylindrical geometry, such that k_y remains a good quantum number, we find the spectra in Fig. 3(b) detailing the absence of gapless states on the x edge. Finally, placing the system in a slab geometry of linear system size $L = 50$ with open boundary conditions along x and y we find the spectra shown in Fig. 3(c), displaying four zero-energy states. The localization of these states at the corners of the sample is shown in Fig. 3(d).

The bulk-boundary correspondence for the corner bound states has been established in prior works through computation of the nested Wilson loop [54,59]. The Wilson loop along direction k_x as a function of k_y, is defined as

$$W_x(k_y) = \mathcal{P}\exp\left[i \oint A_{\mathrm{occ},x}(\mathbf{k}) dk_x\right], \tag{3}$$

where $A_{\mathrm{occ},x}(\mathbf{k}) = -i \langle \Psi_{\mathrm{occ}} | \partial_{k_x} | \Psi_{\mathrm{occ}} \rangle$ is the Berry connection for the occupied subspace. On integration, the Wilson loop can be written in the form,

$$W_x(k_y) = e^{iH_{W,x}(k_y)}. \tag{4}$$

The Wannier center charges (WCCs), $\bar{x}(k_y)$, follow as eigenvalues of $H_{W,x}(k_y)/\pi$ and can be used to determine both the $\mathbb{Z}_2$ index and bulk-boundary correspondence for states on the x edge [12,60,61]. The WCC spectra for Eq. (2) has been shown to be gapped [54–56], indicating a *trivial* $\mathbb{Z}_2$ *index* and lack of gapless topological edge states. The nested Wilson loop follows as the Wilson loop of the Wannier Hamiltonian, $H_{W,x}(k_y)$, and dictates that the corner modes are topologically protected by the presence of quantized quadrupole moment $Q_{xy} = 1/2$ [54]. The quadrupole moment is in turn protected by the presence of chiral symmetry, which has been well documented in Refs. [26,27,54].

Coexisting with the symmetry protected topology of Eq. (2), is nontrivial spin-resolved topology. The spin-resolved topology is identified by a quantized spin-Chern number, $\mathcal{C}_s = (\mathcal{C}_\uparrow - \mathcal{C}_\downarrow)/2$, where $\mathcal{C}_{\uparrow,\downarrow}$ is the Chern number defined for the spin-up and spin-down eigenstate which constitute a Kramers pair. To compute the spin-Chern number we must isolate the spin up(spin down) subsectors of the occupied Kramers pairs. This is accomplished through construction of the projected spin operator (PSO) [25]. The projected spin operator takes the form $\hat{\mathcal{S}} = P(\mathbf{k})\hat{s}P(\mathbf{k})$, where $P(\mathbf{k})$ is the projector onto occupied bands and $\hat{s}$ is a preferred spin axis. In the presence of spin-rotation symmetry it is simple to verify that the eigenvalues of the PSO are fixed as ± 1. The positive(negative) branches of the spectra corresponding to the spin-up(spin-down) eigenstates for which the Chern number, $\mathcal{C}_\uparrow(\mathcal{C}_\downarrow)$, can be computed.

If additional terms violating the spin-rotation symmetry are introduced, then the eigenvalues of the PSO adiabatically deviate from ± 1. So long as a gap in the spectra of the PSO remains present, referred to as the spin gap (labeled Δ_s), $\mathcal{C}_\uparrow(\mathcal{C}_\downarrow)$ can be unambiguously computed. Thus, the spin gap is as fundamental to the problem as the energy gaps. In the presence of disorder, these are converted into energy and spin mobility gaps that have to be determined from quantities that are not self-averaging.

For Eq. (2), a gap in the PSO is present fixing the Fermi energy E/t=0 for the choice, $\hat{s} = s_z = \sigma_3 \otimes \tau_3$, allowing for calculation of the spin-Chern number. The eigenvalues of the spin spectra, as a function of the Fermi energy, are shown in Fig. 4(a), demonstrating that the PSO is gapped for all values of the Fermi energy which fall within the electronic bulk gap.

Computation of the Chern number for the occupied eigenstates of the PSO ($\mathcal{C}_\downarrow$) is accomplished via modification of the coupling matrix method introduced in Ref. [62], replacing the occupied eigenfunctions of the Hamiltonian with the eigenfunctions corresponding to the negative eigenvalues of the PSO. The results establish $\mathcal{C}_s = 1$ for Eq. (2), while we emphasize the absence of a nontrivial $\mathbb{Z}_2$ index.

In correspondence with the presence of a quantized Chern number, the spectral density of the PSO on the surface can be computed for open boundary conditions along x and twisted boundary conditions along y, $\psi(x, y + L) = e^{i\theta_y}\psi(x, y)$. The results in Fig. 4(b) and Fig. 4(c) display the expected spectral flow. Fixing the twist angle, $\theta_y = 0$, we inspect the real space distribution of the eigenstates at $\lambda = 0$ in Fig. 4(d) that demonstrates that these gapless modes are bound to the open edges.

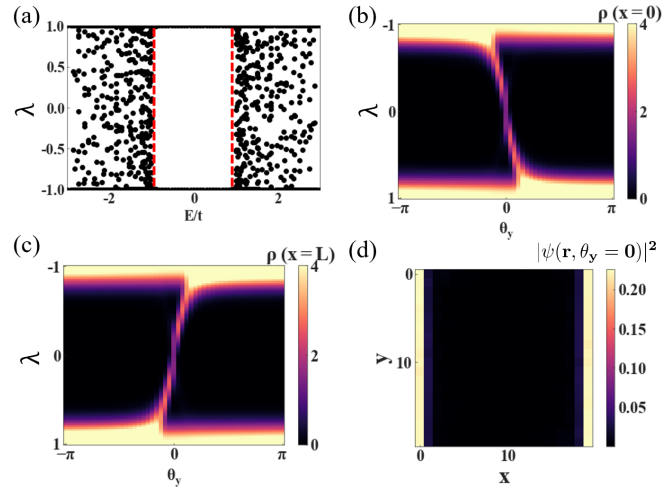

FIG. 4. Properties of the PSO band structure: (a) Spectra of the PSO as a function of the Fermi energy on an $L = 20$ system size with periodic boundary conditions. Red dashed line marks region of energy supporting a gapped PSO spectra. [(b) and (c)] The PSO on an $L = 20$ size system with open boundary conditions along x and twisted boundary conditions along y, for twist θ_y, is considered. The average local density of states on the (b) $x = 0$ and (c) $x = L$ surfaces as a function of the twist angle demonstrating chiral edge states. (d) The real-space distribution of the eigenstates nearest to $\lambda = 0$ for twist angle $\theta_y = 0$, demonstrating localization along the edges.

The analysis of the Bloch Hamiltonian defined in Eq. (2) and presented in this section has established the coexistence of (I) symmetry-protected higher-order topology and (II) spin-resolved topology when the Fermi energy is placed within the bulk gap. The presence of an electronic bulk gap is visible in Fig. 3(a). The electronic gap is marked by red-dashed lines in Fig. 4(a) demonstrating that within this region the PSO is correspondingly gapped. The bulk-boundary correspondence of the symmetry protected higher-order topology has been established through identification of a gap in the surface spectra in Fig. 3(b) and subsequent identification of zero-energy corner localized states as shown in Figs. 3(c) and 3(d). The bulk-boundary correspondence of the PSO as a Chern insulator has been established via analysis of the spectral flow on imposition of twisted boundary conditions as seen in Figs. 4(b) and 4(c). In the following sections we will address whether the gap in the bulk electronic and spin spectrum can be decoupled through introduction of disorder and the corresponding impact on the fate of topological boundary modes.

B. Probes of the disordered model

We now define all quantities computed to construct a complete phase diagram in the presence of disorder.

1. Probes of the energy spectrum and wave functions

To understand the nature of the bulk and surface states we compute the average density of states (DOS), typical density of states (TDOS), and the level statistics through the adjacent gap ratio. It is well known that the DOS cannot distinguish between extended and localized states. By contrast, the TDOS

can distinguish between localized and extended states due to the fact that the TDOS performs a geometric average of the local DOS [57,63,64]. As the electronic states transition from being extended to localized, the local spectrum transitions from continuous to discrete, suppressing the TDOS. As a consequence the TDOS is an appropriate measure of the mobility gap, which can therefore be used to determine the phase boundaries. It is important to stress that on the introduction of disorder the energy gap becomes soft due to nonperturbative Lifshitz states that fill in the gap. Instead, the mobility gap, or the gap in the typical density of states will distinguish metallic and insulating phases. We therefore compute both quantities to develop a full picture of the spectrum of the model. The average DOS is defined as

$$\rho(E) = \frac{1}{L^2}\left[\sum_n \delta(E - E_n)\right], \tag{5}$$

where the sum is over all the eigenstates $|E_n\rangle$ of the Hamiltonian operator H in Eq. (1), $n = 1, \ldots, 4L^2$ for a linear system size L, E_n are the eigenvalues of H, and $[\ldots]$ denotes a disorder average. For the computation of the DOS and TDOS we average over 5000 disorder configurations.

To probe the nature of localized states we define the TDOS through the local DOS via

$$\rho_{\text{typ}}(E) = \exp\left(\frac{1}{4N_s}\sum_{i=1}^{N_s}\sum_{\sigma=1}^{2}\sum_{\tau=1}^{2}[\ln \rho_{i,\sigma,\tau}(E)]\right), \tag{6}$$

where N_s indicates a small collection of random sites considered $N_s \ll L^2$ and the local DOS at site i for spin σ and orbital τ, $\rho_{i,\sigma,\tau}(E)$, is defined as

$$\rho_{i,\sigma,\tau}(E) = \sum_{k,\alpha,\beta} |\langle k, \alpha, \beta | i, \sigma, \tau\rangle|^2 \delta(E - E_{k\alpha\beta}). \tag{7}$$

When examining the surface DOS, the sum over i is restricted to values on the surface of the sample. No such restriction is imposed for the bulk DOS.

In order to correctly ascertain the localization properties it is essential to reach large system sizes. Therefore, both quantities are computed using the KPM [57] for a linear system size of $L = 1000$, this method expands the quantity of interest in terms of Chebyshev polynomials to an order N_C and is able to reach large system sizes by utilizing efficient sparse matrix-vector multiplication. To filter Gibb's oscillations from truncating this series we use the Jackson kernel, which effectively amounts to replacing the Dirac-delta function in the definition of the local DOS in Eq. (7) with a Gaussian of width $\delta E = \pi D/N_C$ [57] and bandwidth D. Once convolved with the wave-function overlap this infrared energy scale δE broadens the effective localization length and therefore scaling with N_C is needed to ascertain localized and delocalized phases [57]. Therefore, in this work we utilize the scaling of the typical DOS with the KPM expansion order (N_C) as a means to probe the localization transitions [57,64]. As we are considering a system of linear size $L = 1000$, we find that the finite-size effects due to the physical system size are minimal at the considered expansion orders (see Appendix A). Rather we must perform scaling with respect to N_c as only in the limit $N_c \to \infty$ does KPM produce an exact result. Truncating N_c to reduce the computational cost then represents the most significant "finite-size" effect, not the physical system size [65]. Due to the convolution of the wave functions and the energy spectrum, the KPM smearing of the energy is turned into a smearing of the wave function. In a metallic phase, the typical DOS will be N_C independent, whereas in the localized phase the typical DOS will be zero in the thermodynamic limit, thus it will go to zero as $N_C \to \infty$ in our numerical simulations on finite size and expansion order. To conclude, we label the gap in the typical DOS as the mobility gap, and strictly speaking there is no gap in the average DOS for any disorder strength.

To provide an additional probe of the delocalized phase and to ascertain its diffusive (i.e., random matrix theory like) metallic properties, the level statistics is computed through the adjacent gap ratio, r_i, and averaged over 500 disorder configurations. We compute the adjacent gap ratio using exact diagonalization from

$$r_i = \frac{\min(\delta_i, \delta_{i+1})}{\max(\delta_i, \delta_{i+1})}, \tag{8}$$

where $\delta_i = E_{i+1} - E_i$ is the difference between neighboring, distinct eigenvalues. In the following, the level statistics is computed as a function of energy that we average over 500 disorder configurations for linear system sizes $L = 20, 40, 60$ that have periodic boundary conditions. The disordered model at hand is in class AI, based on this symmetry classification disorder should be a relevant perturbation and localize all states in the spectrum, which will produce a Poisson distributed adjacent gap ratio $\langle r\rangle \approx 0.386$. However, if the states remain delocalized, which in the current model arises due to purely topological reasons, then the adjacent gap ratio will follow the Gaussian orthogonal ensemble (GOE) [45] random matrix theory ensemble that predicts $\langle r\rangle \approx 0.53$.

2. *Probes of the spin-resolved spectrum and wave functions*

The presence of nontrivial spin-resolved topology is determined by the spectra of the PSO ($\hat{\mathcal{S}}$), which we refer to as the spin spectrum. As we will see, the gap in the spin spectrum is as fundamental to this problem as the electronic spectrum, both must be studied in tandem. We therefore, carefully spell out our analogous approach defining relevant quantities that are similar to the energy spectrum here.

The PSO is a function of the occupied states, fixing a given Fermi energy, E we define the PSO without translational symmetry through

$$\hat{\mathcal{S}} = \hat{P}(E)\hat{s}\hat{P}(E), \tag{9}$$

where $\hat{P}(E)$ projects onto all occupied states up to energy (E), namely $\hat{P}(E) = \sum_{E_n<E} |E_n\rangle\langle E_n|$. From this we define the disorder averaged spin-resolved DOS at the Fermi energy, E, from the spectrum of $\hat{\mathcal{S}}$ through

$$\rho^{\mathcal{S}}(\lambda; E) = \frac{1}{L^2}\left[\sum_n \delta(\lambda - \lambda_n)\right], \tag{10}$$

where λ_n denotes the eigenvalues of $\hat{\mathcal{S}}$ with eigenvectors $|\lambda_n\rangle$ and the sum is over all the eigenvalues $i = 1, \ldots, 4L^2$.

However, its not sufficient to know if the spin spectrum is finite we have to also determine if the spin eigenvectors are

localized in real space or not. Therefore, analogous to the local DOS we define the spin-resolved local DOS at site i for spin σ and orbital τ as

$$\rho^{\mathcal{S}}_{i,\sigma,\tau}(\lambda;E) = \sum_{k,\alpha,\beta} |\langle k,\alpha,\beta|i,\sigma,\tau\rangle|^2 \delta(\lambda - \lambda_{k\alpha\beta}), \quad (11)$$

from which we define the typical spin-resolved DOS,

$$\rho^{\mathcal{S}}_{\text{typ}}(\lambda;E) = \exp\left(\frac{1}{4N_s}\sum_{i=1}^{N_s}\sum_{\sigma=1}^{2}\sum_{\tau=1}^{2}\left[\ln \rho^{\mathcal{S}}_{i,\sigma,\tau}(\lambda;E)\right]\right). \quad (12)$$

Similarly to a metallic and insulating TDOS, we expect that whether the spin-resolved TDOS is nonzero will tell us if the eigenmodes of the PSO are localized or not. Similarly, the gap in the spin-resolved TDOS, we refer to as the spin mobility gap.

In the following we study the spin-resolved spectrum using exact diagonalization and consider system sizes up to $L = 20$. Despite the small sizes we are able to get rather conclusive data on the nature of the PSO in the presence of disorder, which for the present problem has much less severe finite-size effects compared to the eigenstates and spectrum of the Hamiltonian. We remark that it is possible to construct a KPM description of the spin spectrum to reach larger sizes but it requires a double Chebyshev expansion and is therefore left for future development.

3. Topological properties

In the presence of finite disorder we again diagnose bulk topology through computation of the spin-resolved Chern number via a modifying of the coupling matrix method described in Ref. [62]. We emphasize that our implementation differs only through a replacement of the real-space Hamiltonian with the PSO. For clarity, we briefly describe the method.

Defining twisted boundary conditions for single-particle eigenfunctions of the PSO as $\psi(x+L,y) = e^{i\theta_x}\psi(x,y)$ and $\psi(x,y+L) = e^{i\theta_y}\psi(x,y)$ such that $\theta_i \in [0, 2\pi)$. The single-particle eigenfunctions can be Fourier transformed. The twisted boundary conditions impose the constraint that reciprocal space coordinates take on discrete values, $\mathbf{k} = (\frac{2n_1\pi}{L}, \frac{2n_2\pi}{L}) + (\frac{\theta_x}{L}, \frac{\theta_y}{L})$, where $0 \leqslant n_i \leqslant L$.

The Chern number is then computed as

$$C_{\downarrow} = \frac{1}{2\pi i}\oint_{\partial R_q} d\mathbf{l}_q \langle \Phi_q | \nabla_q \Phi_q\rangle, \quad (13)$$

where $|\Phi_q\rangle$ is the Fourier transform of the negative eigenstates of the PSO and ∂R_q is the boundary of the square of side length $2\pi/L$. To carry out the computations we discretize the ∂R_q into 80 segments, replacing the derivative with finite differences. Finally, we average over a minimum of 20 disorder configurations.

III. EFFECTS OF DISORDER

We now come to the effects of disorder when starting from the two-dimensional band structure given by Eq. (2). Importantly, the disorder breaks the translational symmetry and the identification of each phase then follows from the quantities defined in Sec. II B.

A. Bulk and surface electronic phase diagram

1. Insulator with higher-order and spin-resolved topology

We start by establishing the nature of the bulk phase of the model as a function of disorder maintaining the parameter choice, $\Delta_0 = 0$, $t_1 = 0.05$, and $\gamma/\alpha = 0.9$. The TDOS as a function of disorder strength and energy is shown in Fig. 5(a). Importantly, we see a clear mobility gap at weak disorder that does not close as we increase the disorder strength. Instead, we see two clearly metallic bands at finite energies, which Anderson localize around a disorder strength of $W = 1.5$. To mark the mobility edge we follow the procedure outlined in Ref. [66], extrapolating $\rho_{\text{typ}}(E/t)$ to to zero as a function of W for each KPM expansion parameter N_c, identifying the localization transition, $W_l(N_c)$. A second extrapolation is performed to obtain $W_l(N_c)$ in the limit $N_c \to \infty$. Repeating this procedure at each value of E/t produces the phase boundary shown as a dashed white line in Fig. 5(a).

The absence of the closure of the mobility gap is shown clearly through the N_C dependence of $\rho_{\text{typ}}(E=0)$ at the center of the band in Fig. 5(b), where the typical DOS always is a decreasing function of increasing N_C suggesting it is always insulating. However, the average DOS is converged in N_C (on this linear scale) and is always nonzero at finite W, though exponentially small at weak disorder. This gives it an artificial sense of looking like it is lifting off from zero at a particular disorder strength on a linear scale, but in facts its just exponentially small in the disorder strength as expected for Lifshitz states. This is in strong contrast to the localizing behavior seen in the typical DOS.

In contrast, sitting at a finite Fermi energy $E/t = 1.5$, deep in the metallic band, we see a stable metallic phase, which develops a strong N_C dependence at large disorder strength. This is displayed in Fig. 5(c), where the power-law fit to $\rho_{Typ}(E)$ as a function of $\sim(W - W_l(N_C))^x$ to determine an estimate of the localization transition at this expansion order denoted $W_l(N_C)$, which is plotted as black dashed lines. In our data, we find optimal fits for $1.4 < x < 2.0$. The inset then further shows the extrapolation of $W_l(N_C)$ to $N_c \to \infty$ to obtain the result in the thermodynamic limit. Taken together, the results in Fig. 5 clearly show two metallic bands undergoing an Anderson localization transition. If we take a Fermi energy in the mobility gap center, then we see that the localization transition takes place *below the Fermi energy*. This phenomena is quite unlike that of a Chern or $\mathbb{Z}_2$ topological insulator where the mobility gap closes in the band center at a critical disorder strength, namely the delocalization-localization transition takes place at the Fermi energy. Here, for the case of the HOTI, we find that this is no longer the case.

To describe the nature of the metallic phase we turn to the average level statistics on small sizes and the typical DOS at much larger sizes to provide a comparison in Fig. 6. Importantly, we find that the electronic bands have an adjacent gap ratio consistent with the GOE, thus demonstrating a delocalized phase in two dimensions. We emphasize that based solely on symmetry classification, class AI systems in two dimensions are known to be unstable to disorder and localize on introduction of weak disorder in the thermodynamic limit [64,67,68]. Our numerical results provide evidence that the presence of a quantized spin-Chern number serves to obstruct

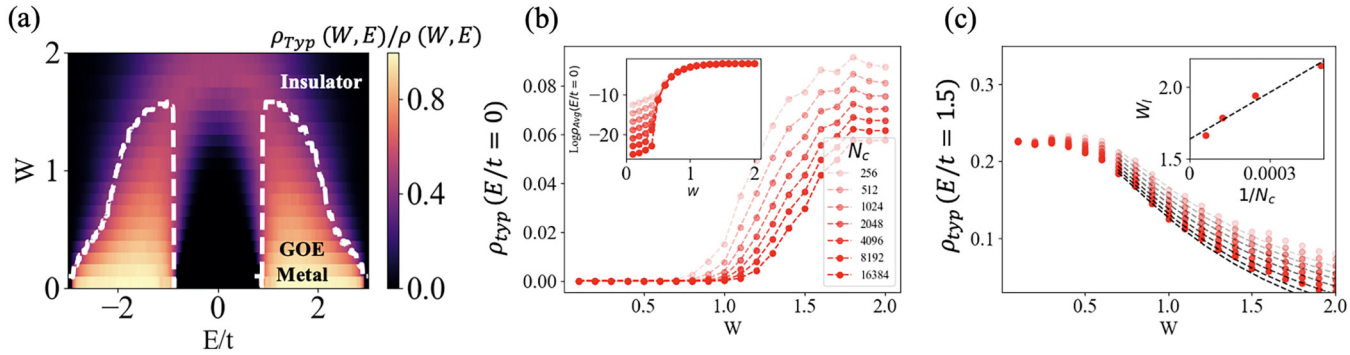

FIG. 5. Typical density of states in the bulk: (a) The ratio of the bulk TDOS defined in Eq. (6) and the average DOS defined in Eq. (5) as a function of disorder strength W and energy E for a fixed system size of $L = 1000$ and KPM expansion order $N_C = 16\,384$. While the data at fixed N_C look like a mobility gap closes, this is not the case as the scaling with N_C needs to be taken into account. The mobility edge is marked by white dashed line. It is computed following the method detailed in (c). (b) Bulk TDOS at zero energy as a function of W for various expansion orders N_C used in the KPM. (c) Bulk TDOS at $E/t = 1.5$ as a function of W for various expansion orders N_C used in the KPM. The localization transition point, $W_l(N_c)$, is determined by extrapolating $\rho_{\text{typ}}(E/t = 1.5)$ to zero. Inset demonstrates extrapolation of $W_l(N_c)$ to $N_c \to \infty$ limit in order to determine the phase boundary.

such localization in the model at hand. One reasonable explanation for this correspondence follows from the fact that topological order is global, not local, and thus generally requires the existence of extended bulk states. This has been previously studied in the context of Wannier representations for crystalline systems [69–72]. In the following section further numerical evidence for the correspondence between a quantized spin-Chern number and extended bulk states will be presented motivating future work towards a rigorous proof of this observation. Importantly, the estimates for the metallic phase boundary obtained via scaling of the TDOS with N_C agrees well with that obtained from the level statistics.

The conclusions we have reached in this subsection do not rely on the higher-order topology of the clean Hamiltonian and instead depend solely on whether topological protection against localization is provided by the spin Chern number $C_s = 1$. We verify this in Appendix C by starting from the spin-resolved topological band structure for which higher-order topology is absent (see the clean phase diagram in Fig. 2), demonstrating that evolution of the level statistics, the mobility gap, and the spin-resolved mobility gap evolve in the same manner as we have shown here. This illustrates that the spin-resolved topological insulators have topologically protected bulk states (that a symmetry analysis would imply are localized) below the Fermi energy. We further demonstrate this principle in Sec. III A 3 below. By removing the spin-resolved topology, we show that the bulk states localize on the introduction of disorder.

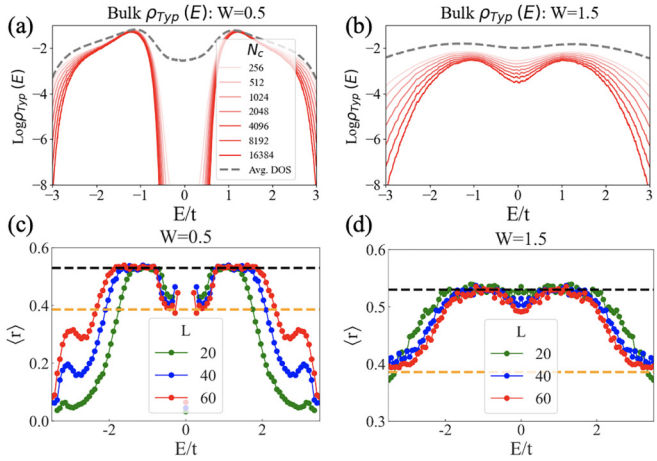

FIG. 6. Revealing the GOE metal at finite energy: Bulk TDOS define in Eq. (6) as a function energy, varying the expansion order, N_C for the kernel polynomial method, fixing the disorder strength to (a) $W = 0.5$ and (b) $W = 1.5$. [(c) and (d)] Adjacent gap ratio defined in Eq. (8) as a function energy for a linear system size L with periodic boundary conditions, fixing the disorder strength (c) $W = 0.5$ and (d) $W = 1.5$ and averaging over 500 disorder configurations. For increasing disorder strength the region supporting finite-energy states that obey the expected result for a GOE, $\langle r \rangle \approx 0.53$ (marked with a black dashed line) becomes sharper. In contrast, in the localized regimes [where we see a strong N_C dependence in (a) and (b)] we also see the level statistics are Poisson (or approaching it) with $\langle r \rangle = 2\log 2 - 1 \approx 0.39$ (marked by dashed orange line) showing the two results are nicely compatible.

2. NATURE OF EDGE MODES

To complete our analysis, we determine the phase diagram of the surface states. It has been established that if the $\mathbb{Z}_2$ index is trivial and spin-Chern number is finite, then helical edge states are not protected. Nevertheless, to complete our analysis and provide a contrast with $\mathbb{Z}_2$ topological insulators it is important to examine the edges at zero and finite energy. To study the edge states at finite energy we impose periodic boundary conditions along the y direction and open boundary conditions along the x direction. We study the surface TDOS by modifying Eq. (6) to restrict the sum over i to lattice sites on the x edge. In Fig. 7(a) we plot the surface TDOS as a function of energy at representative values of disorder strength. We do not find any regime that displays stable metallic surface states and we observe a clear lack of convergence for increasing N_C, that demonstrates the surface states are localized at all energy. To clarify this behavior, we plot the TDOS at $E/t = 0$ and $E/t = 0.5$ as a function of disorder strength in Fig. 7(b) and Fig. 7(c), respectively. At zero energy, the

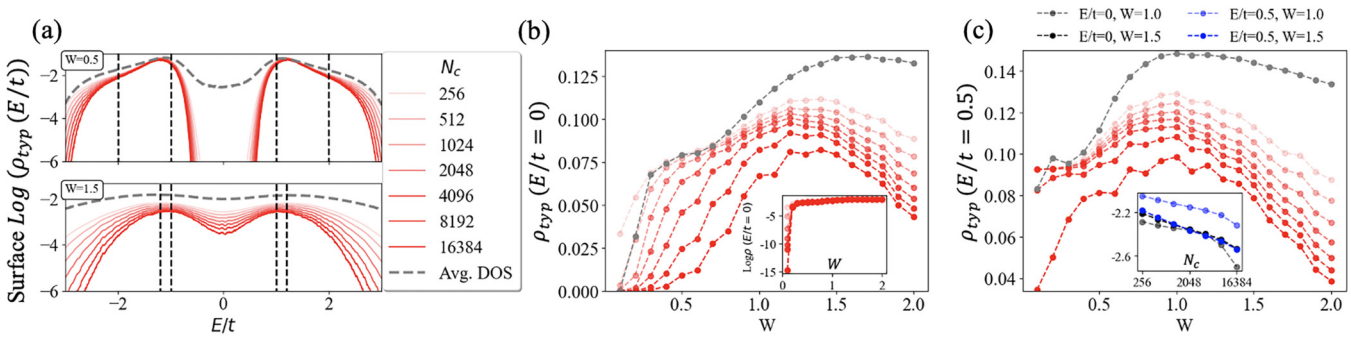

FIG. 7. TDOS computed for sites on an open x surface: We show the TDOS as defined in Eq. (6) as a function of energy, varying the expansion order, N_C for the kernel polynomial method, and fixing the disorder strength to (top) $W = 0.5$ and (bottom) $W = 1.5$. Black dashed lines approximate the location of the bulk mobility gap. (b) Dependence of surface ρ_{typ} as a function of expansion order, N_C, at zero energy. Inset in shows convergence of average DOS at zero energy. (c) Dependence of surface ρ_{typ} as a function of expansion order, N_C, at finite energy. Inset displays N_c dependence at varying energy and disorder strength.

TDOS indicates $\rho_{\text{typ}}(E/t = 0) \to 0$ as $N_C \to \infty$ is always true. By contrast, the ADOS is nonzero at all values of finite disorder, demonstrating the presence of disorder-induced, localized zero-energy states on the surface. These zero-energy states have been the source of speculation that a higher-order to first-order transition can occur. Indeed such a prediction follows naturally from a simple observation that the Bloch Hamiltonian, Eq. (2), admits two masses, $\Delta(\mathbf{k})$ and $M(\mathbf{k})$. While $M(\mathbf{k})$ controls the bulk band gap, $\Delta(\mathbf{k})$ controls the surface gap. We can naively analyze the effects of disorder on these parts of the model within a perturbative (in disorder strength) perspective. Such a Born approximation yields that the effective value of $\Delta(\mathbf{k})$ will vanish prior to that of $M(\mathbf{k})$. However, it is imperative to stress that this perturbative picture is well known to completely fail to explain Anderson localization phenomena [73,74] (and only captures some aspects of the average spectrum), which cannot be described with a perturbative analysis. Importantly, these conclusions are at direct odds with our numerical results as they suggest that protected helical edge states emerge when the effective value of $\Delta(\mathbf{k})$ vanishes, which is simply not the case as we have shown they localize in the presence of disorder. Thus, our analysis unambiguously shows that any disorder-induced zero-energy and finite-energy edge states are *not* topologically protected and no such transition has occurred. Rather, as will be shown, we find the spin gap alone controls the topological classification and existence of extended bulk states. Our numerical data imply that the surface states localize for infinitesimal disorder strength. As a result, it can be concluded that although a quantized spin-Chern number protects the existence of extended bulk states, it does not demand the existence of protected boundary modes, whether at zero or finite energy.

3. Anderson localization in the absence of a spin-Chern number

As stated previously, the model presented falls under class AI in the Altland-Zirnbauer table in the presence of disorder and belongs to the GOE of random matrix theory. We therefore do not expect the bulk, finite-energy metallic phase to be stable to the introduction of disorder [45]. Rather, a symmetry analysis would dictate that the finite-energy bulk metallic phase identified in the clean limit will localize on introduction of infinitesimal disorder. Fascinatingly, we have shown that this is not the observed behavior. Instead the finite-energy bulk GOE metallic phase exhibits stability to disorder as probed via the level statistics and TDOS.

As this result is unexpected based on symmetry classification, it is important to investigate further whether the observed extended states are protected by the existence of nontrivial bulk topology, namely the quantized spin-Chern number. To do so, we can redefine the parameters of the Bloch Hamiltonian in Eq. (2) such that the bulk electronic gap is unchanged, but the spin-Chern number is trivialized. Namely, leaving γ fixed, we tune the value of α such that $|\gamma/\alpha| > 2$, causing the spin-Chern number to vanish (see Fig. 2).

To study the trivial phase sufficiently away from the topological critical point, we fix $\alpha = 0$, keeping all other parameters used in Sec. III A 1 intact. The bulk and surface TDOS as a function of the KPM expansion parameter, N_c, are computed for $W = 0.5$ in a system of size $L = 1000$, averaging over 5000 disorder configurations with the results shown in Fig. 8. In these figures it is clear that for increasing N_c both the bulk and surface TDOS demonstrate convergence towards zero. If we compare this trend at a representative value of energy, $E/t = 1.0$, with the topological system supporting $C_s = 1$, then we find a sharp contrast with the results shown in Fig. 8(c).

In accordance with the analysis presented of the topologically nontrivial model, we compute the level statistics at representative values of disorder strength. As the bulk electronic gap has remained unaffected, we can directly compare the results in Fig. 9 with those in Fig. 6, revealing a stark difference in stability. This behavior provides further evidence for the topological protection of bulk-extended states offered by the spin-Chern number.

B. Bulk and surface spin-resolved phase diagram and topology

Surprisingly, our analysis of the electronic spectrum indicates no extended states are observed at zero energy regardless of the disorder strength. When studying the evolution of a topological insulator as a function of disorder, it is common to focus on the properties of the system at zero energy due to the understanding that the nontrivial topology is protected by

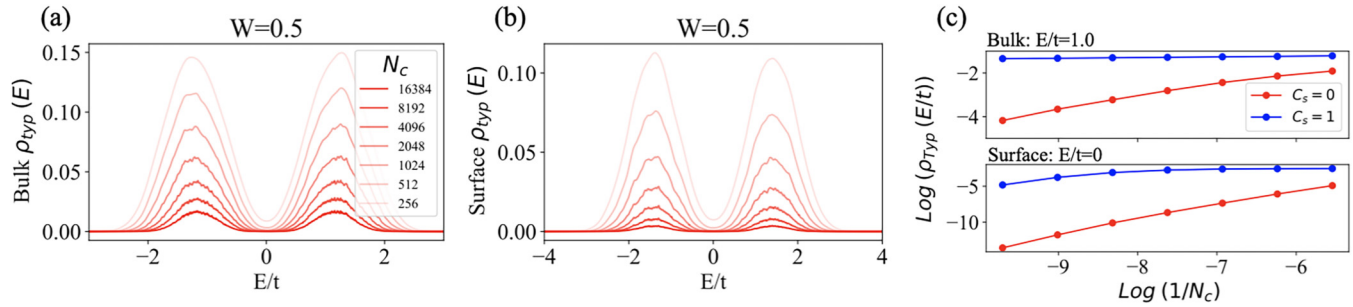

FIG. 8. Typical density of states for trivial insulator. The typical density of states is computed for the trivial insulator supporting $C_s = 0$ as a function of the KPM expansion parameter, N_c. Both the (a) bulk and (b) surface display convergence to zero demonstrating localized states. (c) Comparing the typical density of states as a function of the KPM expansion parameter between a the topological and trivial insulator. The typical density of states at finite energy is vanishing for the trivial insulator and finite for the spin-resolved topological insulator in the bulk while both systems display a vanishing zero-energy typical density of states on the surface.

the bulk-mobility gap. The spin-resolved topological insulator at hand exhibits a strikingly different behavior. Increasing the magnitude of disorder drives a series of metal-insulator transitions at finite energy away from the band center (as shown in Fig. 5). However, in the clean limit in the presence of a finite spin Chern number it is necessary to study both the electronic and spin gap. Therefore, we have generalized each of these theoretical probes from the energy to the spin spectrum in Sec. II B 2 and in this section we turn to a study of the properties of the PSO, for the spin-resolved topological insulating phase realized fixing $\Delta_0 = 0, t_1 = 0.05$ and $\gamma/\alpha = 0.9$, in the presence of disorder.

To do so we first fix the Fermi energy $E = 0$ and compute the TDOS of the PSO for a system size of $L = 20$ under PBCs following Eq. (12), averaging over 50 disorder configurations. The results in Fig. 10(a) are distinct from what was observed for the electronic spectrum in Fig. 5. The spin spectrum supports a spectral gap that narrows with increasing disorder strength and vanishes at $W \approx 1.5$ as shown in Fig. 10(b). Interestingly, this value approximately aligns with the localization of all bulk states.

Next, we consider the effects of varying E, computing the TDOS of the PSO at $\lambda_{\text{PSO}} = 0$ to determine the presence/absence of a spin gap as a function of varying the Fermi energy and disorder strength. The results shown in Fig. 10(c), demonstrate that as disorder strength is increased, the range of E for which a spin gap exists begins to narrow, reflecting the behavior of a familiar Chern insulator. Thus, we have confirmed that the spin mobility gap closes at this topological transition.

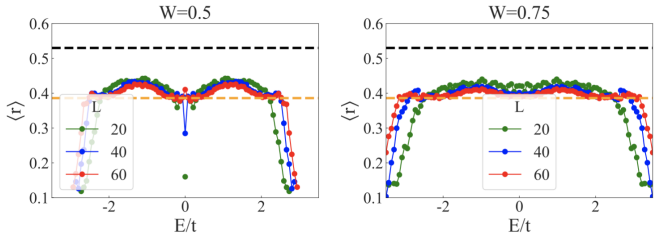

FIG. 9. Topological protection of extended bulk states. By tuning the parameters of Eq. (2), we maintain the bulk electronic gap but access two different topological phases. A symmetry analysis states that neither model will show stability to disorder and the adjacent gap ratio should obey the Poisson distribution with $\langle r \rangle \approx 0.386$, while extended states within the Gaussian orthogonal ensemble are indicated by $\langle r \rangle \approx 0.53$. The disorder averaged adjacent gap ratio for the topological phase is visible in Fig. 6, demonstrating stability to disorder. Results for the topologically trivial model, shown here, clarify that in the absence of topological protection all states localize.

1. Topology of the spin spectrum

The spin-Chern number is expected to remain robust as long as the electronic and spin mobility gaps remain nonzero. It is further reasonable to expect that the spin-Chern number is trivialized on localization of all occupied bulk states in the electronic spectrum. To verify these expectations, we first compute the bulk spin-Chern number fixing $E = 0$. The results shown in Fig. 10(d) demonstrate that as we increase the linear system size, L, the spin-Chern number is quantized for weak disorder, deviating from the quantized value for $W \gtrsim 1.5$. This is in good agreement with the analysis of both the TDOS for the spin and electronic spectrum, demonstrating that the closure of the spin spectral gap and localization of all occupied states are both realized at the same disorder strength (to within our numerical accuracy). To provide further evidence of a sharply defined spin Chern number and the nature of its fluctuations we show the distribution of the spin Chern number across different disorder samples in Fig. 10(e). This reveals that the spin Chern number is quantized for every sample not just on average. As we go through the transition and increase disorder strength this distribution develops a tail towards zero.

Last, we further verify the correspondence between the presence of a mobility gap in the spin spectrum and a quantized spin-Chern number we compute the spin-Chern number as a function of E at representative values of the disorder strength $W = 0.5$ and $W = 1.0$ in Fig. 10(f). The results demonstrate that the spin-Chern number remains quantized when the Fermi Energy (E) is in the electronic and spin mobility gaps.

Having firmly established a direct correspondence between the existence of a spin gap and the existence of a quantized spin-Chern number, a schematic of the bulk phase diagram is constructed. This requires knowledge of the bulk-mobility

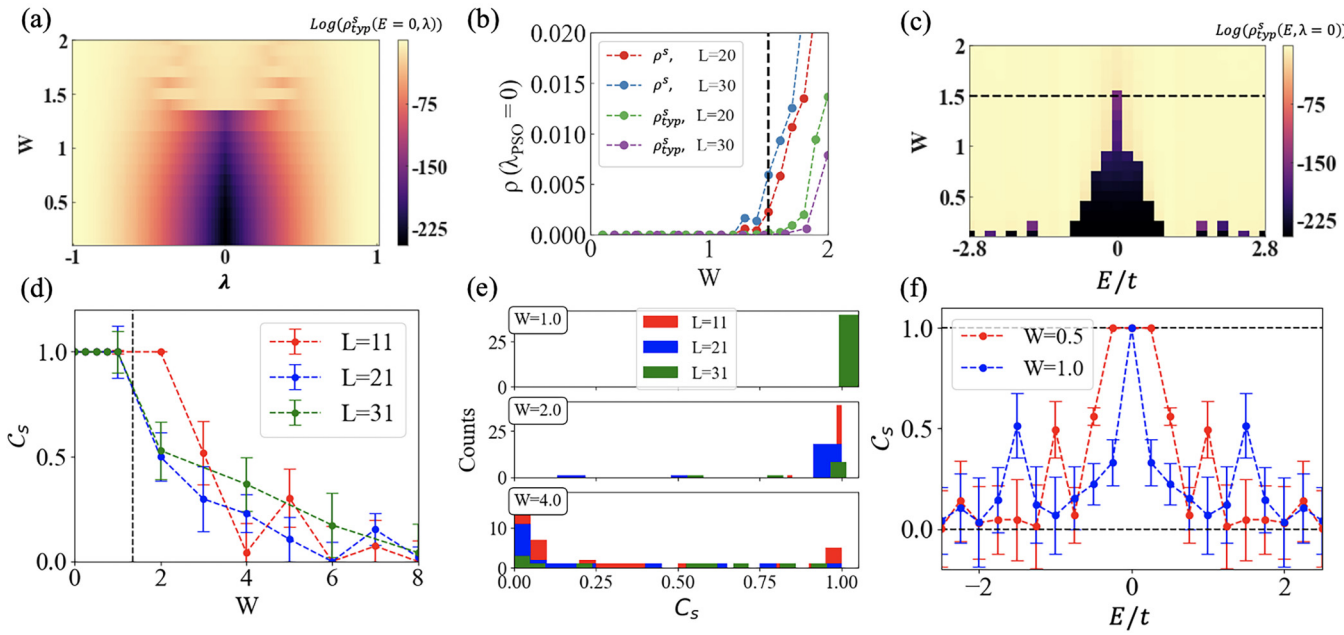

FIG. 10. Disordered properties of the PSO and spin Chern number: (a) Typical density of states of PSO, defined in Eq. (12), at $E = 0$ as a function of magnitude of eigenvalues for the PSO, (λ_{PSO}), and disorder strength under periodic boundary conditions. (b) Typical and average density of states, defined in Eq. (5), of PSO defined at $E = 0$ as a function of disorder strength at $\lambda_{PSO} = 0$. (c) Typical density of states of PSO as a function of disorder strength and Fermi energy at $\lambda_{PSO} = 0$, which shows that it becomes finite wherever the spin gap closes. In each plot a dashed line marks the approximate location at which all occupied states localize in the bulk. (d) Calculation of spin-Chern number, defined in Eq. (13), at the Fermi energy for a supercell of linear size L as a function of disorder strength, averaging over 20 disorder configurations. (e) Histogram detailing results of spin-Chern number computation for individual disorder configurations as a function of disorder strength, fixing $E = 0$. (f) Spin-Chern number as a function of the Fermi energy for representative values of disorder strength.

gap as computed in Fig. 5, as well as knowledge of the spin mobility gap as computed in Fig. 10. The resulting phase diagram, shown in Fig. 1, is striking as it implies the possibility of a topological phase transition, both as a function of the Fermi energy and disorder strength, without closing the mobility gap. However the PSO, which controls the bulk topology, does display such conventional gap closing as seen in Fig. 10(c). It is the hidden nature of the PSO and the interplay between the bulk mobility gap and spin gap which allows for the construction of such an exotic phase diagram.

2. Spin-resolved edge modes

In Sec. III A 2 our computation of the surface TDOS on the edge in a cylindrical geometry led to the conclusion that topological edge states are all localized at any $W > 0$. Nevertheless, it is interesting to investigate the "surface spectra" of the PSO for a fixed E. If we consider the eigenstates associated with the negative (positive) eigenvalues of the PSO to be "occupied" and "unoccupied," then the magnitude of the spin-Chern number corresponds to the magnitude of the Chern number for the "occupied states" of the PSO. As such, for a nonzero quantized spin-Chern number we expect the PSO to support chiral edge modes, a hallmark of the Chern insulator state. We directly examine these edge modes for a system size $L = 20$ in a cylindrical geometry (open boundary conditions along x and twisted boundary conditions along y). We consider representative disorder strengths $W = 1$ and $W = 2$ for which the spin gap has been shown to be open and closed, respectively.

In order to examine the edge modes, we track the local density of states along the $x = 0$ and $x = L$ edges as a function of varying the twisted boundary conditions along y. The results, displayed in Figs. 11(a) and 11(c) for $W = 1$ and Figs. 11(b) and 11(d) for $W = 2$ respectively are in accordance with classification of the PSO as a Chern insulator. For $W = 2$ the spectral flow vanishes indicating the trivial topology. The real-space distribution of the eigenstates nearest to $\lambda = 0$ for $\theta_y = 0$ are also shown in Figs. 11(e) and 11(f) for $W = 1$ and $W = 2$, respectively. These figures underscore that in the topological phase the states are bound to the edge and decouple from the edge in the trivial phase. While the results in Fig. 11 are for single disorder configurations, we have considered 20 possible disorder configurations for each value of W, confirming the results are consistent in each case.

C. Signatures of spin-resolved topology in the electronic spectrum

The previous sections demonstrate that the spin-resolved topological Anderson insulator phase does not admit protected boundary modes at a surface of codimension $n \neq 0$. It is then natural to investigate the case of $n = 0$ through introduction of a zero-dimensional defect in the lattice. The defect we consider is that generated by a dislocation or equivalently insertion of a magnetic flux tube. This is a natural choice as flux insertion is a well-established probe of both Chern

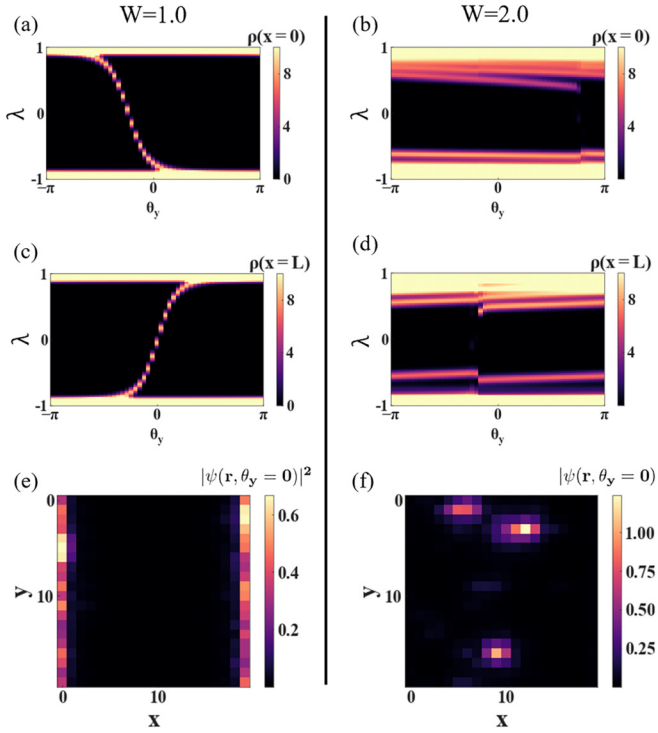

FIG. 11. Surface states of the PSO: The PSO on an $L = 20$ size system with open boundary conditions along x and twisted boundary conditions along y, for twist θ_y, is considered. The average local density of states of the PSO, defined in Eq. (10), on the $x = 0$ surfaces as a function of the twist angle are shown for $W = 1.0$ in (a) and $W = 2.0$ in (b). The average local density of states of the PSO on the $x = L$ surfaces as a function of the twist angle are shown for $W = 1.0$ in (c) and $W = 2.0$ in (c). The results demonstrate the presence (absence) of topological gapless edge modes when a spectral gap is present (absent) in the PSO. The real-space distribution of the eigenstates nearest to $\lambda = 0$ for twist angle $\theta_y = 0$ are given in (e) and (f) for $W = 1$ and $W = 2$, respectively.

insulators and quantum spin-Hall insulators and should allow for the topology of the spin spectrum to be probed through an analysis of the electronic spectrum [41,52,53,75–79].

The magnetic flux tube is placed at the center of the disordered, real-space Hamiltonian of linear system size L, centered at the origin. The presence of a flux tube is simulated using the Peierls substitution with the choice of gauge connection given by

$$A_y = \phi\delta(y)\Theta(x). \tag{14}$$

Imposing a cylindrical geometry we calculate the disorder averaged density of states on the defect, varying the flux strength ϕ from 0 to the flux quanta, $\phi_0 = hc/e$. The results for a linear system size $L = 100$ are shown in Figs. 12(a) and 12(b) for $W = 0.3$ and $W = 0.9$ respectively. The flux tube binds two states which are pumped across the bulk gap as a function of the flux strength.

To understand this behavior, consider first the case where we set $t_1 = 0$ [that is defined in H_0 below Eq. (1)] such that spin-rotation symmetry is preserved. In this case the occupied subspace for $E = 0$ is composed of the occupied subspace of two Chern insulators with $C = \pm 1$. As detailed in Ref. [52],

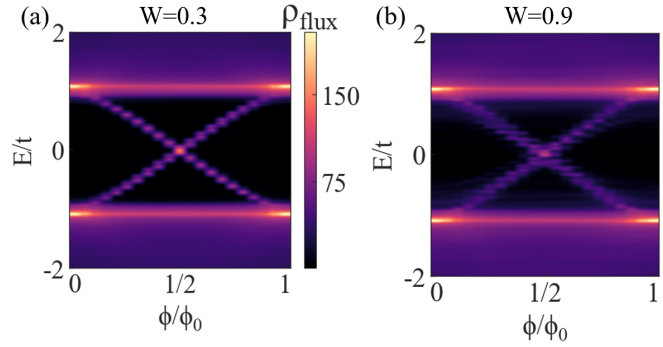

FIG. 12. Probing the topology with a magnetic flux tube: Local density of states on inserted flux tube (ρ_{flux}) as a function of flux strength fixing (a) $W = 0.3$ and (b) $W = 0.9$, considering a linear system size $L = 100$ and averaging over 100 disorder configurations. At $\phi = \phi_0/2$ the modes are degenerate and act in an identical manner to end states of a spinful SSH chain.

for each Chern insulator the adiabatic flux threading process causes $N = |C|$ modes bound to the flux tube to be pumped across the bulk gap. The sign of the Chern number further determines whether these bound modes are pumped from the occupied to unoccupied subspace or vice versa. In the case of a quantum spin-Hall insulator, we therefore observe two counterpropagating flux tube bound modes as a function of flux strength.

On introducing a finite spin-orbit coupling, removing the spin-rotation symmetry, it is possible to gap the degeneracy of the flux tube bound modes seen at $\phi = \phi_0/2$. In the clean limit, for $\Delta_0 = 0$ and $t_1 \neq 0$, this degeneracy is protected by crystalline symmetry [79,80]. For finite disorder, this degeneracy is removed for individual disorder configurations but the states remain bound to the flux tube. When considering a large number of disorder configurations the symmetries are restored in the average [81] and the degeneracy reappears. Regardless of whether such a degeneracy is present, the number of states bound to the inserted flux tube is robust for every disorder configuration and is a known physical observabel of spin-resolved topological insulators, as explored in Ref. [79]. In brief, the flux tube can be used to probe whether the occupied states contain hidden subspaces corresponding to occupied Chern insulating ground states.

IV. DISCUSSION AND CONCLUSION

In this paper we have investigated the effects of quenched short-range potential disorder on the zero temperature phase diagram of two-dimensional $\mathbb{Z}_2$ trivial topological insulators supporting a quantized, finite spin-Chern number.

While we utilize a prototypical model of a higher-order topological insulator as a starting point in the clean limit, it is emphasized that higher-order topology is a separate entity all together and the higher-order classification is immediately trivialized via introduction of disorder. Nevertheless, spin-resolved topology and higher-order topology can be shown to coexist in two dimensions in the clean limit, offering a large class of experimental systems to search for the exotic physics identified in this work.

As a consequence, we expect these results to be relevant in the ongoing studies of two-dimensional higher-order topological insulators [46,79,82,83] as well as fragile topological insulators [79]. The outcome of the present study also shows that midgap, finite-energy edge modes typically identified in two-dimensional, $\mathbb{Z}_2$ trivial materials supporting a spin-Hall conductivity [46,48,49,51] are fragile and will be localized in any realistic sample. Furthermore, our results are directly applicable in the context of two-dimensional heterostructures and twisted (or moiré) materials where additional degrees of freedom such as valley and minivalley, etc., can give rise to pseudo(spin)-resolved topology [84,85]. It will be exciting to see how these conclusions play out when considering three-dimensional systems, which we leave for future work.

Our results expand our fundamental understanding of topological materials and the meaning of "topological protection." By decoupling the spin and bulk spectral gap through disorder, the model yields a phase diagram whereby a topological phase is bordered by a trivial insulating phase without an intervening gapless point. In other words, the bulk mobility gap and the spin mobility gap have decoupled resulting in Anderson localization taking place below the Fermi energy where the topology remains quantized. Furthermore, our results extend the concept of *n*th order insulators in a direction not previously explored, demonstrating that topologically protected boundary modes exist only on a zero-dimensional defect.

ACKNOWLEDGMENTS

We thank Jennifer Cano, Sankar Das Sarma, Taylor Hughes, David Huse, Jay Sau, David Vanderbilt, and Justin Wilson for insightful discussions. This work is partially supported by NSF Career Grant No. DMR- 1941569 and the Alfred P. Sloan Foundation through a Sloan Research Fellowship (C.G. and J.H.P.). Part of this work was performed in part at the Aspen Center for Physics, which is supported by the National Science Foundation Grant No. PHY-2210452 (A.C.T. and J.H.P.) as well as the Kavli Institute of Theoretical Physics that is supported in part by the National Science Foundation under Grants No. NSF PHY-1748958 and No. PHY-2309135 (J.H.P.). A.C.T. acknowledges the hospitality of the Center for Materials Theory at Rutgers University. Nordita is supported in part by NordForsk. A portion of this research was done using services provided by the OSG Consortium [86–89], which is supported by the National Science Foundation Awards No. 2030508 and No. 1836650. The authors acknowledge the Office of Advanced Research Computing (OARC) at Rutgers, The State University of New Jersey for providing access to the Amarel cluster and associated research computing resources that have contributed to the results reported here. A.C.T. acknowledges computational resources provided by the National Academic Infrastructure for Supercomputing in Sweden (NAISS), partially funded by the Swedish Research Council through Grant Agreement No. 2022-06725.

APPENDIX A: SYSTEM-SIZE DEPENDENCE OF THE PHASE DIAGRAM

In order to verify that the finite-size effects in the main body arise due to the KPM expansion order, N_c, and not from the physical system size, L, we consider a system smaller than that used to obtain the results in the main body. Namely, we consider a system of size $L = 500$, the main body utilizes $L = 1000$. The bulk TDOS is then recomputed as a function of varying the Fermi energy, E, as well as the disorder strength, W and the KPM expansion order. We follow the procedure detailed in the main body to systematically obtain the phase boundary. The results in Fig. 13, compare the phase boundary as determined for $L = 500$ with that determined for $L = 1000$. They are overlapping, establishing that our choice of system size, L, does not lead to finite-size effects in computation of the TDOS and construction of the phase diagram.

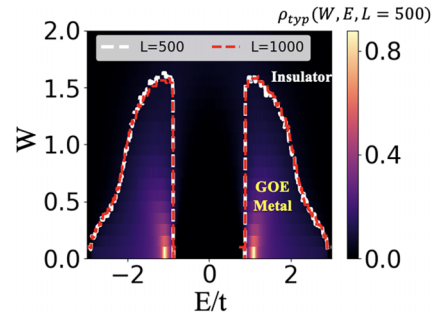

FIG. 13. Typical density of states in the bulk for $L = 500$. The bulk TDOS as a function of disorder strength, W and energy E for a fixed system size of $L = 500$ and KPM expansion order $N_C = 16\,384$. The mobility edge computed for $L = 500$ and $L = 1000$ are marked by white and red dashed lines respectively.

APPENDIX B: NATURE OF THE CORNER MODES WHEN HIGHER-ORDER TOPOLOGY IS PRESENT IN CLEAN LIMIT

As stated in the main body, higher-order topology is not a requirement to realize a system in which $C_s = 1$ and $\mathbb{Z}_2 = 0$. However in the clean limit these topological properties can be identified in two-dimensional higher-order topological insulators. It is therefore useful to examine the presence/absence of protected corner states to provide a comprehensive study of the bulk-boundary correspondence in spin-resolved topological insulators. The robustness of corner modes to the introduction of disorder in two-dimensional HOTIs has been studied for alternate models [90,91]. Such studies are broadly interested in maintaining the bulk-corner correspondence of HOTIs as dictated by topological invariants protected by symmetries that may be removed through the inclusion of disorder. For the model utilized in this work, Eq. (2), the bulk invariant protecting the corner modes is a quantized quadrupole moment, Q_{xy}. As stated in Sec. II A, quantization of the quadrupole moment is protected by chiral symmetry, in the clean limit. Introduction of onsite disorder removes the chiral symmetry. It is therefore expected that corner modes will not be protected. Furthermore, infinitesimal disorder populates the edge gap with localized states, the combination of this fact with the removal of crystalline symmetries disallows topological classification via the filling anomaly.

To investigate the fate of the corner modes on introduction of disorder when $\Delta_0 = 0, t_1 = 0.05$ and $\gamma/\alpha = 0.9$, we consider the four lowest-lying states of a two-dimensional slab of

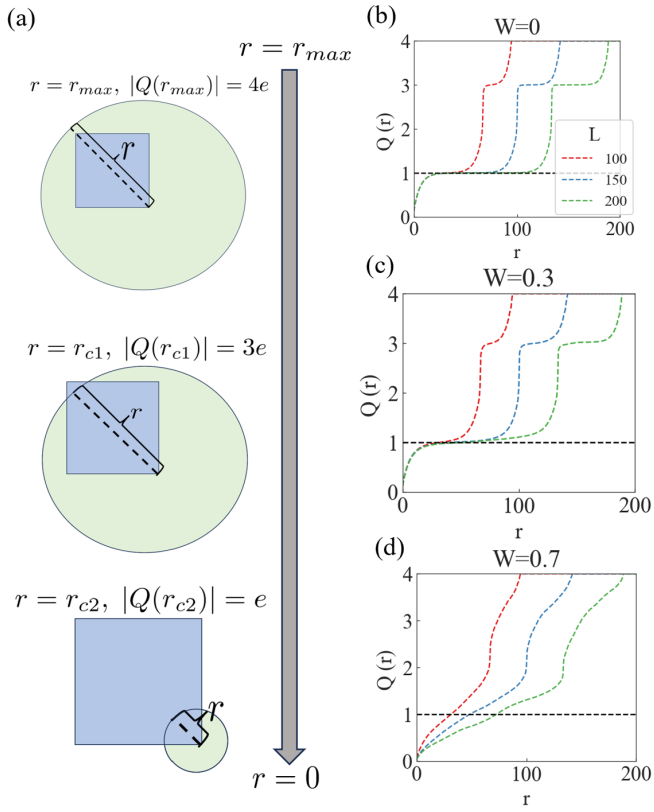

FIG. 14. Delocalization of the corner charge: (a) Schematic detailing measurement of corner bound charge. Charge density within a circle of radius, r, centered at a corner is computed. $Q(r)$, defined in Eq. (B1), exhibits three main features: If r is large enough to contain the full system, then $Q(r) = 4e$; if r is decreased such that only three corners are contained within the circle, then $Q(r) = 3e$, two corners of the square are then removed simultaneously providing a third transition to $Q(r) = e$. [(b)–(d)] Charge contained with a circle of radius r centered about a corner of a two-dimensional slab of size L^2 with open-boundary conditions. We consider the four lowest-lying states as a function of disorder strength, averaging over 100 disorder configurations. Quantization of corner charge is destroyed by increasing of the disorder strength, indicating that corner localized modes are not protected from disorder.

size L^2 at $L = 100, 150, 200$ with open boundary conditions along both the x and y directions using Lanczos [92]. The charge localized at the corner is computed as

$$Q(r)/e = \sum_{\mathbf{r}'_i < r} \sum_{n=1}^{4} |\psi_n(\mathbf{r}'_i)|^2, \tag{B1}$$

where the sums are over the four lowest-lying state and $\mathbf{r}'_i$ indicates distance from the bottom right corner of the two-dimensional slab. A schematic of the expected behavior in the clean limit is shown in Fig. 14(a).

The results in Figs. 14(b)–14(d) demonstrate that in the presence of disorder charge quantization at the corners is destroyed. This is in accordance with the removal of the underlying symmetry protected topology and further demonstrates that topologically protected boundary modes, whether at a surface of codimension one or two, are absent.

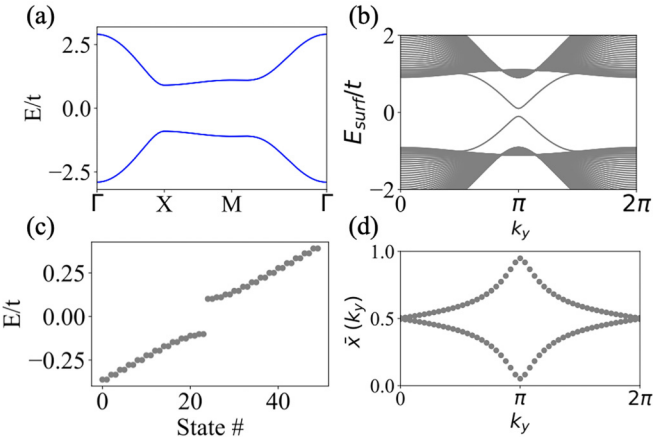

FIG. 15. Properties of the clean band structure: (a) Bulk band structure on fixing $\Delta_0 = 0.1$, $t_1 = 0$, and $\gamma/\alpha = 0.9$ in Eq. (2). (b) Spectra of nanoribbon, composed of 40 unit cells along the x direction as a function of momenta, k_y, displaying absence of gapless edge states. (c) Spectrum for slab of size $L = 50$ with open boundary conditions, detailing absence of corner localized modes. (d) Wannier center charge spectra demonstrating trivial nature of $\mathbb{Z}_2$ index.

APPENDIX C: SPIN-RESOLVED TOPOLOGICAL INSULATOR WITHOUT HIGHER-ORDER TOPOLOGY IN THE CLEAN LIMIT

In the main body we utilize, as a starting point for investigation of a $\mathbb{Z}_2$ trivial insulator supporting a quantized spin-Chern number, a prototypical model of a spinful higher-order topological insulator supporting bulk-corner correspondence [56,93]. Higher-order topological insulators represent a natural class of systems to identify such physics as the general principal of construction for higher-order topological systems relies on addition of a $\mathcal{T}$-odd axion mass to a Dirac Hamiltonian describing a first-order topological insulator [94]. This axion mass has the effect of gapping the surface states and removing classification as a nontrivial $\mathbb{Z}_2$ insulator. However, the axion mass does not have the effect of closing the spin gap, indicating that the spin-Chern number will remain robust. This is the reason spin-Hall conductivity has been used as an effective computational probe in the search for higher-order topological insulators [46].

Nevertheless, in the clean limit, an additional topologically nontrivial phase is visible in Fig. 2 which lacks higher-order topology while supporting $C_s = 1$. To demonstrate that it is solely the spin-resolved topology which is responsible for the physics observed in this work, we consider a model formed via the parameter choice $\Delta_0 = 0.1$, $t_1 = 0.0$, and $\gamma/\alpha = 0.9$ in Eq. (2). This choice places us in the topologically nontrivial phase in the bottom right of Fig. 2. The bulk band structure is shown in Fig. 15(a) demonstrating that it is an insulator. The absence of gapless edge modes is shown for a nanoribbon spectra in Fig. 15(b) and the absence of corner modes is shown plotting the lowest energy states for a slab of size $L = 50$ with open boundary conditions in Fig. 15(c). By computing the

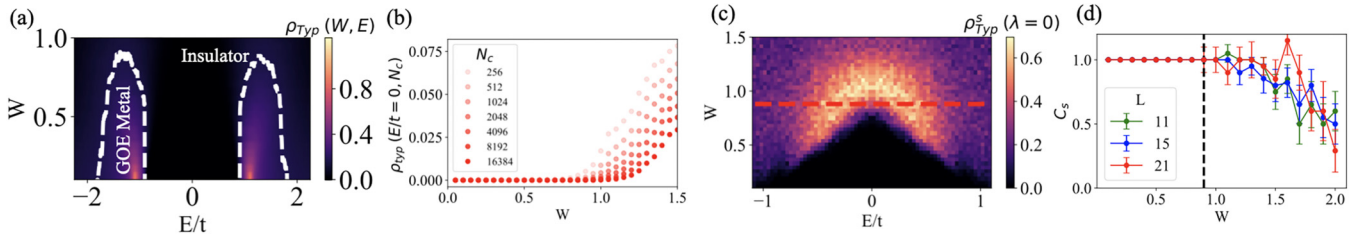

FIG. 16. Effects of disorder: (a) The bulk TDOS as a function of disorder strength, W and energy E for a fixed system size of $L = 500$ and KPM expansion order $N_C = 16\,384$. The mobility edge is marked by white dashed line, computed following the power-law fitting procedure detailed in the main body. (b) Bulk TDOS at $E/t = 0$ as a function of W for various expansion orders (N_C) used in the KPM. A strong N_c dependence is visible, indicating the presence of localized states for all values of disorder strength. (c) Typical density of states for the spin-spectrum band center, $\lambda = 0$, as a function of the electronic Fermi energy and disorder strength. Red dashed line indicates disorder strength at which all electronic states localize. (d) Disorder averaged spin-Chern number, considering 50 disorder configurations, as a function of disorder strength. Vertical black dashed line indicates location at which electronic states localize. Error bars detail the standard error for the disorder configurations.

Wannier center charge spectra, visible in Fig. 15(d) we can confirm that it is gapped and that the $\mathbb{Z}_2$ classification is trivial. However, by computing the spin-Chern number, for choice of spin-quantization axis $\hat{s} = \sigma_3 \otimes \tau_3$, we find $C_s = 1$.

Having established that this parameter choice removes the higher-order topology while maintaining the classification $C_s = 1$, we perform a brief analysis of disorder effects. As in the main body, at each site, we model the quenched disorder as a random onsite potential $V(\mathbf{r})$. We sample the potential $V(\mathbf{r})$ from a Gaussian distribution with zero mean and variance W^2, and hence W characterizes the strength of disorder; W will be expressed in units of t.

We first consider the effects of disorder on the electronic spectra by computing the TDOS for the electronic and spin spectra. The TDOS for the electronic spectra is computed as a function of the disorder strength using KPM for a system of size $L = 500$ and varying the KPM expansion order, N_c. The results shown in Fig. 16(a) reveal a series of finite-energy metal-insulator transitions as a function of the disorder strength, with all occupied states demonstrating localization for $W \sim 0.9$. Furthermore, Fig. 16(b) demonstrates a strong N_c dependence for the TDOS at zero energy, indicating that *the bulk-mobility gap does not close*.

We then examine the spin-spectra TDOS computed for a system of size $L = 20$, averaging over 50 disorder configurations as a function of the Fermi energy at $\lambda = 0$. The results are shown in Fig. 16(c). This figure demonstrates that the spin mobility gap closes at $W \approx 0.9$ when the Fermi energy is set to zero. This is in agreement with a computation of the spin-Chern number, utilizing the coupling matrix method discussed in the main body, and averaging over 50 disorder configurations, shown in Fig. 16(d). The spin-Chern number is quantized for every disorder configuration when $W < 0.9$. The correspondence between the value of disorder strength at which all states localize and trivialization of the spin-Chern number supports the conclusion that extended bulk states are protected by the spin-resolved topology.

In addition to the TDOS, for the bulk electronic spectra we compute the the disorder averaged adjacent gap ratio, $\langle r \rangle$ as a function of energy and disorder strength, averaging over 500 disorder configurations for a system of size $L = 60$. In the limit of extended states we expect $\langle r \rangle \approx 0.53$ for the GOE, while for localized states the system should obey a Poisson distribution and support $\langle r \rangle \approx 0.386$. The results are compared with the TDOS at representative values of disorder strength in Fig. 17 showing excellent agreement.

1. Nature of edge modes

We now focus on the nature of edge modes in the presence of disorder. As stated in the main body, despite lacking protected helical edge states as would be found in the presence of a nontrivial Z_2 index, in the clean limit finite-energy edge

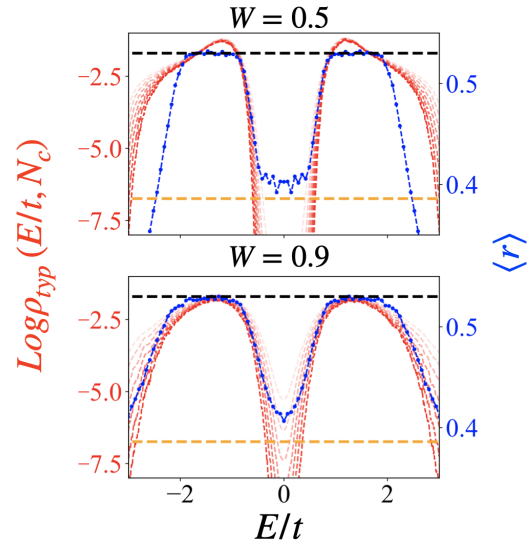

FIG. 17. Finite-energy GOE metal: Bulk TDOS as a function of energy, varying the expansion order, N_C, for the kernel polynomial method, fixing the disorder strength to (upper) $W = 0.5$ and (lower) $W = 0.9$ is compared with the adjacent gap ratio for a linear system size $L = 60$ with periodic boundary conditions, averaging over 500 disorder configurations. For increasing disorder strength the region supporting finite-energy states that obey the expected result for a GOE, $\langle r \rangle \approx 0.53$ (marked with a black dashed line) becomes sharper. In contrast, in the localized regimes [where we see a strong N_C dependence] we also see the level statistics are Poisson (or approaching it) with $\langle r \rangle = 2\log 2 - 1 \approx 0.39$ (marked by dashed orange line) showing the two results are nicely compatible.

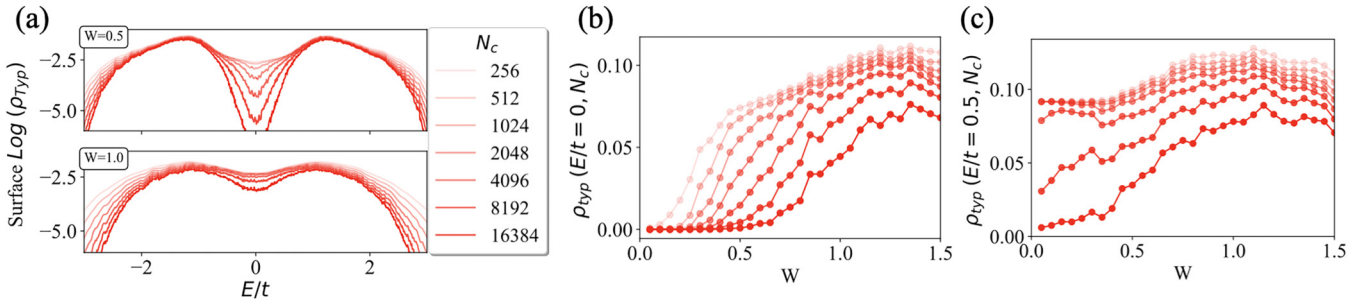

FIG. 18. TDOS computed for sites on an open x surface: We show the TDOS as defined in Eq. (6) as a of function energy, varying the expansion order, N_C, for the kernel polynomial method and fixing the disorder strength to (top) $W = 0.5$ and (bottom) $W = 1.0$. (b) Dependence of surface ρ_{typ} as a function of expansion order, N_C, at zero energy. (c) Dependence of surface ρ_{typ} as a function of expansion order, N_C, at finite energy.

bound states can be found within the bulk gap. This is visible in Fig. 15(b).

To study the edge modes we follow the procedure laid out in the main body, imposing periodic boundary conditions along the y direction and open boundary conditions along the x direction. We then compute the TDOS but restrict the sum over lattice sites to only include sites on the x edge. In Fig. 18(a) the surface TDOS is shown as a function of energy at representative values of disorder strength. The results display a significant dependence on the KPM expansion parameter, N_c, indicating lack of a stable metallic phase. We further plot the TDOS at $E/t = 0.0$ and $E/t = 0.5$ as a function of the disorder strength and KPM expansion parameter in Fig. 18(b) and Fig. 18(c), respectively. These figures demonstrate that the surface TDOS converges to zero as $N_c \to \infty$, leading to the conclusion that despite the presence of topologically protected extended bulk states, topologically protected boundary modes are absent. This is a unique feature of the disordered, spin-resolved topological insulator.

In summary, this example underscores the fact that decoupling of the spin-Chern number and electronic gap requires only absence of a nontrivial $\mathbb{Z}_2$ index and quantized C_s. Any additional topological classification, such as the presence of higher-order topology, is not strictly necessary.

[1] K. v. Klitzing, G. Dorda, and M. Pepper, New method for high-accuracy determination of the fine-structure constant based on quantized Hall resistance, Phys. Rev. Lett. **45**, 494 (1980).

[2] D. J.Thouless, M. Kohmoto, M. P. Nightingale, and M. den Nijs, Quantized Hall conductance in a two-dimensional periodic potential, Phys. Rev. Lett. **49**, 405 (1982).

[3] C. L. Kane and E. J. Mele, Z_2 topological order and the quantum spin Hall effect, Phys. Rev. Lett. **95**, 146802 (2005).

[4] B. A. Bernevig, T. L. Hughes, and S.-C. Zhang, Quantum spin Hall effect and topological phase transition in HgTe quantum wells, Science **314**, 1757 (2006).

[5] M. Z. Hasan and C. L. Kane, *Colloquium:* Topological insulators, Rev. Mod. Phys. **82**, 3045 (2010).

[6] X.-L. Qi and S.-C. Zhang, Topological insulators and superconductors, Rev. Mod. Phys. **83**, 1057 (2011).

[7] R. B. Laughlin, Anomalous quantum Hall effect: An incompressible quantum fluid with fractionally charged excitations, Phys. Rev. Lett. **50**, 1395 (1983).

[8] J. Eisenstein and H. Stormer, The fractional quantum Hall effect, Science **248**, 1510 (1990).

[9] F. D. M. Haldane, Model for a quantum Hall effect without Landau levels: Condensed-matter realization of the "parity anomaly," Phys. Rev. Lett. **61**, 2015 (1988).

[10] D. J. Thouless, Anderson's theory of localized states, J. Phys. C: Solid State Phys. **3**, 1559 (1970).

[11] F. Klopp, Weak disorder localization and Lifshitz tails, Commun. Math. Phys. **232**, 125 (2002).

[12] L. Fu and C. L. Kane, Topological insulators with inversion symmetry, Phys. Rev. B **76**, 045302 (2007).

[13] X.-L. Qi, T. L. Hughes, and S.-C. Zhang, Topological field theory of time-reversal invariant insulators, Phys. Rev. B **78**, 195424 (2008).

[14] C. Xu and J. E. Moore, Stability of the quantum spin Hall effect: Effects of interactions, disorder, and $\mathbb{Z}_2$ topology, Phys. Rev. B **73**, 045322 (2006).

[15] S. Ryu, C. Mudry, H. Obuse, and A. Furusaki, $\mathbb{Z}_2$ topological term, the global anomaly, and the two-dimensional symplectic symmetry class of anderson localization, Phys. Rev. Lett. **99**, 116601 (2007).

[16] A. P. Schnyder, S. Ryu, A. Furusaki, and A. W. W. Ludwig, Classification of topological insulators and superconductors, AIP Conf. Proc. **1134**, 10 (2009).

[17] R. Shindou and S. Murakami, Effects of disorder in three-dimensional Z_2 quantum spin Hall systems, Phys. Rev. B **79**, 045321 (2009).

[18] S. Ryu, A. P. Schnyder, A. Furusaki, and A. W. Ludwig, Topological insulators and superconductors: Tenfold way and dimensional hierarchy, New J. Phys. **12**, 065010 (2010).

[19] G. Schubert, H. Fehske, L. Fritz, and M. Vojta, Fate of topological-insulator surface states under strong disorder, Phys. Rev. B **85**, 201105(R) (2012).

[20] B. Leung and E. Prodan, Effect of strong disorder in a three-dimensional topological insulator: Phase diagram and maps of the $\mathbb{Z}_2$ invariant, Phys. Rev. B **85**, 205136 (2012).

[21] K. Kobayashi, T. Ohtsuki, and K.-I. Imura, Disordered weak and strong topological insulators, Phys. Rev. Lett. **110**, 236803 (2013).

[22] T. Morimoto and A. Furusaki, Stability of surface states of weak $\mathbb{Z}_2$ topological insulators and superconductors, Phys. Rev. B **89**, 035117 (2014).

[23] H. Katsura and T. Koma, The $\mathbb{Z}_2$ index of disordered topological insulators with time reversal symmetry, J. Math. Phys. **57**, 021903 (2016).

[24] C.-K. Chiu, J. C. Y. Teo, A. P. Schnyder, and S. Ryu, Classification of topological quantum matter with symmetries, Rev. Mod. Phys. **88**, 035005 (2016).

[25] E. Prodan, Robustness of the spin-Chern number, Phys. Rev. B **80**, 125327 (2009).

[26] C.-A. Li, B. Fu, Z.-A. Hu, J. Li, and S.-Q. Shen, Topological phase transitions in disordered electric quadrupole insulators, Phys. Rev. Lett. **125**, 166801 (2020).

[27] Y.-S. Hu, Y.-R. Ding, J. Zhang, Z.-Q. Zhang, and C.-Z. Chen, Disorder and phase diagrams of higher-order topological insulators, Phys. Rev. B **104**, 094201 (2021).

[28] C. Wang and X. R. Wang, Disorder-induced quantum phase transitions in three-dimensional second-order topological insulators, Phys. Rev. Res. **2**, 033521 (2020).

[29] J.-H. Wang, Y.-B. Yang, N. Dai, and Y. Xu, Structural-disorder-induced second-order topological insulators in three dimensions, Phys. Rev. Lett. **126**, 206404 (2021).

[30] C. Wang and X. R. Wang, Robustness of helical hinge states of weak second-order topological insulators, Phys. Rev. B **103**, 115118 (2021).

[31] Y. Shen, Z. Li, Q. Niu, and Z. Qiao, Disorder-induced phase-transitions in three-dimensional chiral second-order topological insulator, arXiv:2308.02256.

[32] Y.-L. Tao, J.-H. Wang, and Y. Xu, Average symmetry protected higher-order topological amorphous insulators, SciPost Phys. **15**, 193 (2023).

[33] Y.-R. Ding, D.-H. Xu, and C.-Z. Chen, Disorder-induced phase transitions in higher-order nodal line semimetals, arXiv:2401.13443.

[34] Y.-B. Yang, J.-H. Wang, K. Li, and Y. Xu, Higher-order topologicalphases in crystalline and non-crystalline systems: A review, J. Phys.: Condens. Matter **36**, 283002 (2024).

[35] Z. Su, Y. Kang, B. Zhang, Z. Zhang, and H. Jiang, Disorder induced phase transition in magnetic higher-order topological insulator: A machine learning study, Chin. Phys. B **28**, 117301 (2019).

[36] A. Agarwala, V. Juričić, and B. Roy, Higher-order topological insulators in amorphous solids, Phys. Rev. Res. **2**, 012067(R) (2020).

[37] T. Peng, C.-B. Hua, R. Chen, Z.-R. Liu, H.-M. Huang, and B. Zhou, Density-driven higher-order topological phase transitions in amorphous solids, Phys. Rev. B **106**, 125310 (2022).

[38] N. Okuma, M. Sato, and K. Shiozaki, Topological classification under nonmagnetic and magnetic point group symmetry: Application of real-space Atiyah-Hirzebruch spectral sequence to higher-order topology, Phys. Rev. B **99**, 085127 (2019).

[39] J. Yi and C. Q. Chen, Delocalization and higher-order topology in a nonlinear elastic lattice, New J. Phys. **26**, 063004 (2024).

[40] T. Nag, V. Juričić, and B. Roy, Out of equilibrium higher-order topological insulator: Floquet engineering and quench dynamics, Phys. Rev. Res. **1**, 032045(R) (2019).

[41] B. Roy and V. Juričić, Dislocation as a bulk probe of higher-order topological insulators, Phys. Rev. Res. **3**, 033107 (2021).

[42] A. L. Szabó and B. Roy, Dirty higher-order Dirac semimetal: Quantum criticality and bulk-boundary correspondence, Phys. Rev. Res. **2**, 043197 (2020).

[43] S. Manna, S. Nandy, and B. Roy, Higher-order topological phases on fractal lattices, Phys. Rev. B **105**, L201301 (2022).

[44] M. Li, D. Zhirihin, M. Gorlach, X. Ni, D. Filonov, A. Slobozhanyuk, A. Alù, and A. B. Khanikaev, Higher-order topological states in photonic kagome crystals with long-range interactions, Nat. Photon. **14**, 89 (2020).

[45] W. Buijsman, V. Cheianov, and V. Gritsev, Random matrix ensemble for the level statistics of many-body localization, Phys. Rev. Lett. **122**, 180601 (2019).

[46] M. Costa, G. R. Schleder, C. Mera Acosta, A. C. Padilha, F. Cerasoli, M. Buongiorno Nardelli, and A. Fazzio, Discovery of higher-order topological insulators using the spin Hall conductivity as a topology signature, npj Comput. Mater. **7**, 49 (2021).

[47] T. P. Cysne, M. Costa, L. M. Canonico, M. B. Nardelli, R. B. Muniz, and T. G. Rappoport, Disentangling orbital and valley Hall effects in bilayers of transition metal dichalcogenides, Phys. Rev. Lett. **126**, 056601 (2021).

[48] M. Costa, B. Focassio, L. M. Canonico, T. P. Cysne, G. R. Schleder, R. B. Muniz, A. Fazzio, and T. G. Rappoport, Connecting higher-order topology with the orbital Hall effect in monolayers of transition metal dichalcogenides, Phys. Rev. Lett. **130**, 116204 (2023).

[49] B. Wang, Y.-C. Hung, X. Zhou, A. Bansil, and H. Lin, Higher-order topological phases hidden in quantum spin Hall insulators, Phys. Rev. B **108**, 245103 (2023).

[50] T. P. Cysne, M. Costa, M. B. Nardelli, R. B. Muniz, and T. G. Rappoport, Ultrathin films of black phosphorus as suitable platforms for unambiguous observation of the orbital Hall effect, Phys. Rev. B **108**, 165415 (2023).

[51] B. Wang, X. Zhou, Y.-C. Hung, Y.-C. Lin, H. Lin, and A. Bansil, High spin-Chern-number insulator in α-antimonene with a hidden topological phase, 2D Mater. **11**, 025033 (2024).

[52] X.-L. Qi and S.-C. Zhang, Spin-charge separation in the quantum spin Hall state, Phys. Rev. Lett. **101**, 086802 (2008).

[53] Y. Ran, A. Vishwanath, and D.-H. Lee, Spin-charge separated solitons in a topological band insulator, Phys. Rev. Lett. **101**, 086801 (2008).

[54] W. A. Benalcazar, B. A. Bernevig, and T. L. Hughes, Quantized electric multipole insulators, Science **357**, 61 (2017).

[55] W. A. Benalcazar, T. Li, and T. L. Hughes, Quantization of fractional corner charge in C_n-symmetric higher-order topological crystalline insulators, Phys. Rev. B **99**, 245151 (2019).

[56] M. Ezawa, Edge-corner correspondence: Boundary-obstructed topological phases with chiral symmetry, Phys. Rev. B **102**, 121405(R) (2020).

[57] A. Weiße, G. Wellein, A. Alvermann, and H. Fehske, The kernel polynomial method, Rev. Mod. Phys. **78**, 275 (2006).

[58] E. Khalaf, W. A. Benalcazar, T. L. Hughes, and R. Queiroz, Boundary-obstructed topological phases, Phys. Rev. Res. **3**, 013239 (2021).

[59] F. Schindler, A. M. Cook, M. G. Vergniory, Z. Wang, S. S. P. Parkin, B. A. Bernevig, and T. Neupert, Higher-order topological insulators, Sci. Adv. **4**, eaat0346 (2018).

[60] T. L. Hughes, E. Prodan, and B. A. Bernevig, Inversion-symmetric topological insulators, Phys. Rev. B **83**, 245132 (2011).
[61] M. Taherinejad, K. F. Garrity, and D. Vanderbilt, Wannier center sheets in topological insulators, Phys. Rev. B **89**, 115102 (2014).
[62] Y.-F. Zhang, Y.-Y. Yang, Y. Ju, L. Sheng, R. Shen, D.-N. Sheng, and D.-Y. Xing, Coupling-matrix approach to the Chern number calculation in disordered systems, Chin. Phys. B **22**, 117312 (2013).
[63] V. Dobrosavljević, A. Pastor, and B. Nikolić, Typical medium theory of Anderson localization: A local order parameter approach to strong-disorder effects, Europhys. Lett. **62**, 76 (2003).
[64] J. H. Pixley, P. Goswami, and S. Das Sarma, Anderson localization and the quantum phase diagram of three dimensional disordered Dirac semimetals, Phys. Rev. Lett. **115**, 076601 (2015).
[65] J. H. Pixley, D. A. Huse, and S. Das Sarma, Uncovering the hidden quantum critical point in disordered massless Dirac and Weyl semimetals, Phys. Rev. B **94**, 121107(R) (2016).
[66] J. H. Pixley, D. A. Huse, and S. Das Sarma, Rare-region-induced avoided quantum criticality in disordered three-dimensional Dirac and Weyl semimetals, Phys. Rev. X **6**, 021042 (2016).
[67] A. Altland, Low-energy theory of disordered graphene, Phys. Rev. Lett. **97**, 236802 (2006).
[68] I. L. Aleiner and K. B. Efetov, Effect of disorder on transport in graphene, Phys. Rev. Lett. **97**, 236801 (2006).
[69] N. Marzari and D. Vanderbilt, Maximally localized generalized Wannier functions for composite energy bands, Phys. Rev. B **56**, 12847 (1997).
[70] N. Marzari, A. A. Mostofi, J. R. Yates, I. Souza, and D. Vanderbilt, Maximally localized Wannier functions: Theory and applications, Rev. Mod. Phys. **84**, 1419 (2012).
[71] T. Thonhauser and D. Vanderbilt, Insulator/Chern-insulator transition in the Haldane model, Phys. Rev. B **74**, 235111 (2006).
[72] A. A. Soluyanov and D. Vanderbilt, Wannier representation of $\mathbb{Z}_2$ topological insulators, Phys. Rev. B **83**, 035108 (2011).
[73] C. W. Groth, M. Wimmer, A. R. Akhmerov, J. Tworzydło, and C. W. J. Beenakker, Theory of the topological Anderson insulator, Phys. Rev. Lett. **103**, 196805 (2009).
[74] D. Xu, J. Qi, J. Liu, V. Sacksteder, X. C. Xie, and H. Jiang, Phase structure of the topological Anderson insulator, Phys. Rev. B **85**, 195140 (2012).
[75] V. Juričić, A. Mesaros, R.-J. Slager, and J. Zaanen, Universal probes of two-dimensional topological insulators: Dislocation and π flux, Phys. Rev. Lett. **108**, 106403 (2012).
[76] A. Mesaros, R.-J. Slager, J. Zaanen, and V. Juričić, Zero-energy states bound to a magnetic π-flux vortex in a two-dimensional topological insulator, Nucl. Phys. B **867**, 977 (2013).
[77] F. Schindler, S. S. Tsirkin, T. Neupert, B. Andrei Bernevig, and B. J. Wieder, Topological zero-dimensional defect and flux states in three-dimensional insulators, Nat. Commun. **13**, 5791 (2022).
[78] A. C. Tyner and P. Goswami, Spin-charge separation and quantum spin Hall effect of β-bismuthene, Sci. Rep. **13**, 11393 (2023).
[79] K.-S. Lin, G. Palumbo, Z. Guo, Y. Hwang, J. Blackburn, D. P. Shoemaker, F. Mahmood, Z. Wang, G. A. Fiete, B. J. Wieder *et al.*, Spin-resolved topology and partial axion angles in three-dimensional insulators, Nat. Commun. **15**, 550 (2024).
[80] A. C. Tyner, S. Sur, D. Puggioni, J. M. Rondinelli, and P. Goswami, Topology of three-dimensional Dirac semimetals and generalized quantum spin Hall systems without gapless edge modes, Phys. Rev. Res. **5**, L012019 (2023).
[81] R. Ma and C. Wang, Average symmetry-protected topological phases, Phys. Rev. X **13**, 031016 (2023).
[82] J. Sødequist, U. Petralanda, and T. Olsen, Abundance of second order topology in C_3 symmetric two-dimensional insulators, 2D Mat. **10**, 015009 (2022).
[83] A. C. Tyner and P. Goswami, Solitons and real-space screening of bulk topology of quantum materials, arXiv:2304.05424.
[84] K. F. Mak, K. L. McGill, J. Park, and P. L. McEuen, The valley Hall effect in MoS_2 transistors, Science **344**, 1489 (2014).
[85] Z. Tao, B. Shen, W. Zhao, N. C. Hu, T. Li, S. Jiang, L. Li, K. Watanabe, T. Taniguchi, A. H. MacDonald *et al.*, Giant spin Hall effect in AB-stacked $MoTe_2/WSe_2$ bilayers, Nat. Nanotechnol. **19**, 28 (2024).
[86] R. Pordes, D. Petravick, B. Kramer, D. Olson, M. Livny, A. Roy, P. Avery, K. Blackburn, T. Wenaus, F. Wurthwein *et al.*, The open science grid, J. Phys.: Conf. Ser. **78**, 012057 (2007).
[87] I. Sfiligoi, D. C. Bradley, B. Holzman, P. Mhashilkar, S. Padhi, and F. Wurthwein, The pilot way to grid resources using glideinWMS, *2009 WRI World Congress on Computer Science and Information Engineering* (2009), Vol. 2, pp. 428–432.
[88] OSG, Ospool, OSG 344 (2006), 10.21231/906P-4D78.
[89] OSG, Open science data federation. OSG 344 (2015), https://doi.org/10.21231/0KVZ-VE57.
[90] H. Araki, T. Mizoguchi, and Y. Hatsugai, Phase diagram of a disordered higher-order topological insulator: A machine learning study, Phys. Rev. B **99**, 085406 (2019).
[91] A. K. Ghosh, T. Nag, and A. Saha, Floquet second-order topological Anderson insulator hosting corner localized modes, Phys. Rev. B **110**, 125427 (2024).
[92] C. Lanczos, An iteration method for the solution of the eigenvalue problem of linear differential and integral operators, J. Res. Natl. Bur. Stand. **45**, 255 (1950).
[93] W. A. Benalcazar, B. A. Bernevig, and T. L. Hughes, Electric multipole moments, topological multipole moment pumping, and chiral hinge states in crystalline insulators, Phys. Rev. B **96**, 245115 (2017).
[94] D. Călugăru, V. Juričić, and B. Roy, Higher-order topological phases: A general principle of construction, Phys. Rev. B **99**, 041301(R) (2019).